Detailed Spectroscopic and Theoretical Studies on $[Fe(EDTA)(O_2)]^{3-}$: Electronic Structure of the Side-on Ferric−Peroxide Bond and Its Relevance to Reactivity

Frank Neese and Edward I. Solomon*

Contribution from the Department of Chemistry, Stanford University, Stanford, California 94305

Received May 5, 1998

Abstract: A spectroscopic study of the Fe(III)−EDTA−peroxide complex using electron paramagnetic resonance (EPR), low-temperature absorption (LT-ABS), variable-temperature−variable-field (VTVH) magnetic circular dichroism (MCD), and resonance Raman (rR) spectroscopies is reported. Density functional (DFT) and INDO/S-CI molecular orbital (MO) calculations are used to derive an experimentally calibrated bonding scheme. The molecule is described as a 6-coordinate, mononuclear, high-spin ferric−peroxide complex with a side-on η^2-FeO_2 arrangement. EPR spectroscopy shows that the zero-field splitting (ZFS) is negative with $D = -1.0 \pm 0.25$ cm^{-1} and $E/D = 0.21$. MCD and LT-ABS spectroscopies lead to the identification of at least six excited states below 35 000 cm^{-1}. The lowest two are assigned as ligand field sextet→quartet transitions, and the remaining transitions have peroxide to iron ligand-to-metal charge transfer (LMCT) character. The polarization of the LMCT bands in the principal axis system of the **D**-tensor are derived by VTVH-MCD spectroscopy. The Fe−O and O−O stretching vibrations are observed at 459 and 816 cm^{-1}, respectively. rR excitation profiles are simulated to obtain excited-state distortions. The weak CT bands in the visible region mainly enhance the O−O stretch, whereas the UV band dominantly enhances the metal−ligand stretch and only weakly the O−O stretch. A normal coordinate analysis shows little mechanical coupling between the two stretches and gives force constants of 3.02 mdyn/Å for the O−O stretch and 1.56 mdyn/Å for the Fe−O stretch. MO calculations show that the bonding is dominated by a strong, covalent σ-bond formed between the Fe-d_{xy} and peroxide-π^*_σ orbitals with little contributions from π- or δ-symmetry iron−peroxide interactions. A back-bonding interaction between Fe-3d and the peroxide-σ*-orbital that contributes to the weak O−O bond in oxyhemocyanin is not present in the Fe(III)−EDTA−peroxide complex. A calculation of the **D**-tensor from the INDO/S-CIS(D) wave functions gives good agreement with the experimental values and defines the orientation of the **D**-tensor in the molecular coordinate system. This allows the polarizations obtained from VTVH-MCD spectroscopy to be related to a molecular axis system and assists in band assignments. The negative *D*-value and the observed excited distortions are explained by the extensive anisotropic covalency of the FeO_2 σ-bond. Possible contributions of the electronic structure to the reactivity of non-heme iron enzymes are considered, and protonation of the peroxide ligand is proposed to lead to highly reactive species.

Introduction

Non-heme iron (NH−Fe) enzymes are involved in a wide variety of biological transformations, many of which involve the activation and cleavage of the double bond of O_2.[1] The enzymes with mononuclear active sites contain divalent or trivalent iron in the resting state, and they are thought to function by either of two mechanisms. In one, substrate reacts with the ferric center to be activated for attack by dioxygen as in the proposed reaction cycles of lipoxygenase[2] and protocatechoate 3,4-dioxygenase.[3] The second involves reaction of dioxygen with the ferrous active site to produce an oxygen intermediate that attacks the substrate. In the latter case, the primary ferrous-dioxygen (or ferric-superoxo) adduct is thought to be further reduced by 1 electron to generate a ferric−peroxide-level intermediate. This type of reaction is exemplified by the DNA-cleaving glycopeptide bleomycin.[4]

Oxygen activation by heme enzymes has been studied in much more detail than for non-heme systems and is generally believed to proceed via the pathway in Scheme 1.[5]

In this scheme, obligate intermediates are a ferric-peroxo (or hydroperoxo) species as well as a high-valent iron-oxo species that has been formulated as porphyrin-radical−$(FeO)^{2+}$ (com-

(1) (a) Feig, A. L.; Lippard, S. J. *Chem. Rev.* **1994**, *94*, 759. (b) Que, L. Jr. In *Active Oxygen in Biochemistry*; Valentine, J. S., et al., Eds.; Blackie Academic & Professional: New York, 1995; pp 232−275. (c) Que, L. Jr.; Ho, R. Y. N. *Chem. Rev.* **1996**, *96*, 2607. (d) Wallar, B. J.; Lipscomb, J. D. *Chem Rev.* **1996**, *96*, 2625. (e) Ho, R. Y. N.; Liebman, J. F., Valentine, J. S. In *Active Oxygen in Biochemistry*; Valentine, J. S., et al., Eds.; Blackie Academic & Professional: New York, 1995; pp 1−83.

(2) (a) Solomon, E. I.; Zhou, J.; Neese, F.; Pavel, E. G. *Chem. Biol.* **1997**, *11*, 795. (b) Veldink, G. A.; Vliegenthardt, J. F. G. *Adv. Inorg. Biochem.* **1984**, *6*, 139. (c) Nelson, M. J.; Seitz, S. P. *Curr. Opin. Struct. Biol.* **1994**, 878.

(3) (a) Lipscomb, J. D.; Orville, A. M. *Metals Biol. Syst.* **1992**, *28*, 243. (b) Que, L. Jr. In *Iron Carriers and Iron Proteins*; Loehr, T. M., Ed.; VCH: New York, 1992; pp 469−524.

(4) (a) Stubbe, J.; Kozarich, J. W. *Chem. Rev.* **1987**, *87*, 1107. (b) Stubbe, J.; Kozarich, J. W.; Wu, W.; Vanderwall, D. E. *Acc. Chem. Res.* **1996**, *29*, 322. (c) Hecht, S. M. *Acc. Chem. Res.* **1986**, *19*, 383.

(5) (a) Traylor, T. G.; Traylor, P. S. In *Active Oxygen in Chemistry and Biology*; Blackie Academic and Professional: New York, 1995; pp 84−188. (b) Groves, J. T. *J. Chem. Educ.* **1985**, *62*, 928. (c) Dawson, J. H. *Science* **1988**, *240*, 433. (d) Sono, M.; Roach, M. P.; Coulter, E. D.; Dawson, J. H. *Chem. Rev.* **1996**, *96*, 2841. (e) *Cytochrome P450: Structure, Mechanism and Biochemistry*; Ortiz-de Montellano, P. R., Ed.; Plenum: New York, 1985.

10.1021/ja981561h CCC: $15.00
Published on Web 12/01/1998

Scheme 1

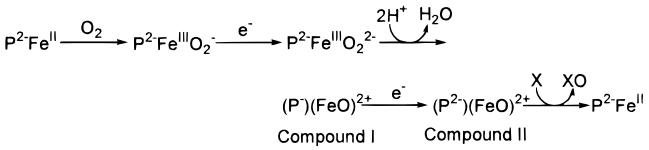

pound **I**) and its 1-electron-reduced form (compound **II**). The most active species is compound **II**, which is thought to transfer oxygen atoms to organic substrates either directly or by a rebound mechanism.[5] Peroxide-level intermediates as well as high-valent iron−porphyrin species have been observed in heme model chemistry, heme-catalases, and peroxidases and have been strongly implicated for cytochrome P450.[5,6]

In relation to mononuclear NH−Fe sites, a significant point of discussion has been whether high-valent iron-oxo intermediates could also exist in their reaction cycles. These intermediates have been proposed for α-keto-acid−dependent enzymes,[1b,c,7] Rieske dioxygenases,[8] bleomycin,[9] and isopenicilin synthase[10] but have never been observed spectroscopically. Whether a high-valent iron species can be formed depends on the properties of the ferric−peroxide precursor, which must allow for heterolytic cleveage of the O−O bond, and on the ability of the ligand environment to stabilize the high-valent species in a biologically significant redox potential range.[11]

Clearly, the electronic structure of ferric−peroxide-level intermediates should be a major determinant that controls the molecular mechanism of reaction. However, only a few mononuclear ferric−peroxide complexes have been reported that are stable enough for detailed investigation by physical methods. Most of these are heme systems,[6h,f,12] where the intense absorptions of the porphyrin moiety obscure many of the interesting spectroscopic features that might be attributed to the ferric−peroxide bond. In addition, charge delocalization into the porphyrin ring is expected to significantly alter the properties of the Fe−O_2 bond relative to non-heme species.

We have therefore decided to study the purple species that is formed on the addition of either H_2O_2 to Fe(III)−EDTA or KO_2 to Fe(II)−EDTA at elevated pH as a classic example of a non-heme ferric−peroxide complex. The complex, which was discovered in 1956, has found use in analytical chemistry[13] and as a catalyst for styrene polymerization.[14] Fe(III)−EDTA also catalyzes superoxide dismutation,[15] hydrogen peroxide decomposition[16,17] and organic substrate oxidation in the presence of H_2O_2.[16] It has therefore been attractive as a mimic of the superoxide dismutase, catalase, and peroxidase enzymes and, consequently, detailed kinetic information is available.[15−17] The Fe(III)−EDTA−peroxide complex has been studied by a variety of spectroscopic methods,[13,16,18] which have demonstrated that it is a 1:1 adduct and that it exists in an $S = {}^5/_2$ ground state, the latter indicating that a ferric−peroxide rather than a ferrous-superoxide description is appropriate.

The binding mode of the peroxo ligand has previously been addressed by resonance Raman (rR) spectroscopy with the use of mixed isotope ($H^{16}O^{18}OH$) hydrogen peroxide.[18b] The absence of an isotope splitting on the ν_{OO} stretching mode observed at 815 cm^{-1} has been taken as definitive evidence for a side-on (η^2) peroxide coordination geometry. This binding mode, which is frequently referred to as the Griffith mode,[19] is frequently observed in complexes of early transition metals with peroxide[20] and has also been implicated for some porphyrin−peroxo complexes.[12f,21] Although it constitutes one of the fundamental possibilities of peroxide−ferric binding geometries, the electronic properties of this η^2-O_2^{2-}−Fe(III) bond are not yet sufficiently understood to allow for a correlation between structure, spectroscopy, and reactivity.[22]

This paper presents a detailed study of the ground and excited states of the Fe(III)−EDTA−peroxide complex by a variety of spectroscopic methods, including electron paramagnetic resonance (EPR), low-temperature absorption (LT-ABS), rR isotope shifts and excitation profiles, and variable-temperature−variable-

(6) (a) Dunford, H. B.; Stillman, J. S. *Coord. Chem. Rev.* **1976**, *19*, 187. (b) Edwards, S. L.; Nguyen, H. X.; Hamlin, R. C.; Kraut, J. *Biochemistry* **1987**, *26*, 1503. (c) Fulop, V.; Phizackerly, R. P.; Aoltis, S. M.; Clifton, I. J.; Wakatsuki, S.; Erman, J.; Edwards, S. L. *Structure* **1994**, *2*, 201. (d) Baek, H. K.; Van Wart, H. E. *J. Am. Chem. Soc.* **1992**, *114*, 718. (e) Loew, G. H.; Harris, D. L. *J. Am. Chem. Soc.* **1996**, *118*, 10588. (f) Balch, A. L. *Inorg. Chim. Acta* **1992**, *198−200*, 297. (g) Sawyer, D. T.; Sugimoto, H.; Tung, H. C. In *The Role of Oxygen in Chemistry and Biochemistry*; Ando, W.; Moro-Oka, Y., Eds.; Elsevier Science: Amsterdam, 1988; 407. (h) Arasingham, R. D.; Balch, A. L.; Latos-Grazynski, L. In *The Role of Oxygen in Chemistry and Biochemistry*; Ando, W.; Moro-Oka, Y., Eds.; Elsevier Science: Amsterdam, 1988; p 417.

(7) (a) Pascal, R. A.; Oliver, M. A.; Chen, Y. C. *Biochemistry* **1985**, *24*, 3158. (b) Townsend, C. A.; Basak, A. *Tetrahedron* **1991**, *47*, 2591.

(8) (a) Wende, P.; Bernhardt, F. H.; Pfleger, K. *Eur. J. Biochem.* **1989**, *181*, 189. (b) Ballou, D. P.; Batie, C. In *Oxidases and Related Redox Systems*; King, T. E., et al., Eds.; Alan R. Liss: New York, 1988; p 211.

(9) Murugesan, N.; Hecht, S. M. *J. Am. Chem. Soc.* **1985**, *107*, 493.

(10) (a) Baldwin, J. E.; Adlington, R. M.; Domayne-Hayman, B. P.; Knight, G.; Ting, H. H. *J. Chem. Soc. Chem. Commun.* **1989**, 1661. (b) Baldwin, J. E.; Bradley, M. *Chem. Rev.* **1990**, *90*, 1079. (c) Baldwin, J. E.; Lynch, G. P.; Schofield, C. J. *J. Chem. Soc. Chem. Commun.* **1991**, 36. (d) Baldwin, J. E.; Adlington, R. M.; Bradley, M.; Pitt, A. R.; Turner, N. J. *J. Chem. Soc. Chem. Commun.* **1989**, 978.

(11) Lippard, S. J.; Berg, J. M. *Principles of Bioinorganic Chemistry*; University Science Books: Mill Valley, 1994.

(12) (a) McCandlish, E.; Miksztal, A. R.; Nappa, M.; Sprenger, A. Q.; Valentine, J. S.; Stong, J. D.; Spiro, T. G. *J. Am. Chem. Soc.* **1980**, *102*, 4268. (b) Miksztal, A. R.; Valentine, J. S. *Inorg. Chem.* **1984**, *23*, 3548. (c) Burstyn, J. N.; Roe, J. A.; Miksztal, A. R.; Shaevitz, B. A.; Lang, G.; Valentine, J. S. *J. Am. Chem. Soc.* **1988**, *110*, 1382. (d) Ozawa, S.; Watanabe, Y.; Morishima, I. *Inorg. Chem.* **1994**, *33*, 306. (e) Dickman, M. H.; Pope, M. T. *Chem. Rev.* **1994**, *94*, 569. (f) Friant, P.; Goulden, J.; Fischer, J.; Ricard, L.; Schappacher, M.; Weiss, R.; Momentou, M. *Nouv. J. Chim.* **1985**, *9*, 33.

(13) (a) Cheng, K. L.; Lott, P. F. *Anal. Chem.* **1956**, *28*, 462. (b) Ringbom, A.; Saxen, B. *Anal. Chim. Acta* **1957**, *16*, 541. (c) Kachanova, Z. P.; Purmal, A. P. *Russ. J. Phys. Chem.* **1964**, *38*, 1342.

(14) Bond, J.; Brown, C. W.; Rushton, G. S. *Polymer Lett.* **1964**, *2*, 1015.

(15) (a) McClune, G. J.; Fee, J. A.; McClusky, G. A. Groves, J. T. *J. Am. Chem. Soc.* **1977**, *99*, 5220. (b) Bull, C.; McClune, G. J.; Fee, J. A. *J. Am. Chem. Soc.* **1983**, *105*, 5290.

(16) (a) Walling, C.; Kurz, M.; Schugar, H. J. *Inorg. Chem.* **1970**, *9*, 931. (b) Walling, C. *Acc. Chem. Res.* **1975**, *8*, 125. (c) Walling, C.; Partch, R. E.; Weil, T. *Proc. Natl. Acad. Sci. U.S.A.* **1975**, *72*, 140. (d) Walling, C.; Kato, S. *J. Am. Chem. Soc.* **1971**, *93*, 4275. (e) Marusak, R. A.; Mears, C. F. In: *Active Oxygen in Biochemistry;* Valentine, J. S., et al., Eds.; Blackie Academic and Professional: London, 1995; pp 336−400.

(17) (a) Orhanovic, M.; Wilkins, R. G. *Croat. Chim. Acta* **1967**, *39*, 149. (b) Rizkalla, E. N.; El-Shafey, O. H.; Guindy, N. M. *Inorg. Chim. Acta* **1982**, *57*, 199. (c) Francis, K. C.; Cummins, D.; Oakes, J. *J. Chem. Soc., Dalton Trans.* **1985**, 493. (d) Mader, P. M. *J. Am. Chem. Soc.* **1960**, *82*, 2956. (e) Rush, J. D.; Koppenol, W. H. *J. Inorg. Biochem.* **198**, *29*, 199. (f) Selbig, S.; van Eldik, R. *Inorg. Chem.* **1997**, *36*, 4115 (g) Anis, S. S.; Mansouir, M. A. *Int. J. Chem. Kinet.* **1991**, *23*, 389.

(18) (a) Hester, R. E.; Nour, E. M. *J. Raman Spectrosc.* **1981**, *11*, 35. (b) Ahmad, S.; McCallum, J. D.; Shiemke, A. K.; Appelman, E. H.; Loehr, T. M.; Sanders-Loehr, J. *Inorg. Chem.* **1988**, *27*, 2230. (c) Fuji, S.; Ohya-Nishiguchi, H.; Hirota, N. *Inorg. Chim. Acta* **1990**, *175*, 27. (d) Kochanny, G. L. Jr.; Timnick, A. *J. Am. Chem. Soc.* **1961**, *83*, 2777.

(19) Griffiths, J. S. *Proc. R. Soc. London A* **1956**, *235*, 23.

(20) (a) Dickman, M. H.; Pope, M. T. *Chem. Rev.* **1994**, *94*, 569. (b) Butler, A.; Clague, M. J.; Meister, G. E. *Chem. Rev.* **1994**, *94*, 625. (c) Pecoraro, V. L.; Baldwin, M. J.; Gelasco, A. *Chem. Rev.* **1994**, *94*, 807. (d) Vaska, L. *Acc. Chem. Res.* **1976**, *9*, 175.

(21) Vanatta, R. B.; Strouse, C. E.; Hanson, L. K.; Valentine, J. S. *J. Am. Chem. Soc.* **1987**, *109*, 1425.

(22) For some MO results see (a) Bytheway, I.; Hall, M. B. *Chem. Rev.* **1994**, *94*, 639. (b) Gubelmann, M. H.; Williams, A. F. *Struct. Bonding* **1983**, *55*, 1. (c) Yamaguchi, K.; Takada, K.; Otsuji, Y.; Mizuno, K. In *Organic Peroxides*; Ando, W., Ed.; John Wiley: Chichester, UK, 1992; pp 1−100. (d) Boca, R. *Coord. Chem. Rev.* **1983**, *50*, 1.

field (VTVH) magnetic circular dichroism (MCD). All of the spectra have been subjected to theoretical simulations to effectively parameterize the spectroscopic data. At the next level of analysis, the spectral parameters were calculated by semiempirical INDO/S-CI and density functional (DFT) molecular orbital (MO) methods and analyzed in terms of their bonding origin. The detailed picture of the electronic structure of the complex that emerges is strongly supported by the experimental data. We also present the application of two new methods of analysis. The first is the direct calculation of zero-field splitting (ZFS) tensors from self-consistent field (SCF)-MO−CI wave functions, which allows the explicit inclusion of anisotropic covalency; the second is an analysis of VTVH-MCD data in terms of transition polarizations, which allows one to obtain polarized spectra on randomly oriented molecules in frozen solution. Finally, we discuss the reactivity of the Fe(III)−EDTA−peroxide complex in terms of its electronic structure and its possible relevance to catalysis by NH−Fe enzymes.

Materials and Methods

Substances. All reagents were of the highest grade commercially available and were used without further purification. Unless otherwise noted, Fe(III)−EDTA was prepared by adding the appropriate amount of solid $FeCl_3$ (Fisher Scientific, Fair Lawn, NJ) to CHES (Sigma Chemical Co., St Louis, MO)-buffered solutions (250 mM, pH 11−11.5) that contained at least a 2-fold excess EDTA (Mallinckrodt). After the formation of Fe(III)−EDTA, the pH was readjusted to 11−11.5. The peroxo complex, formed by addition of an ∼5−10-fold excess of H_2O_2 (Mallinckrodt) over iron, was stable at room temperature for ∼10 min. For low-temperature spectroscopy, samples were quickly frozen in liquid nitrogen to prevent sample decomposition. ^{18}O-enriched H_2O_2 was synthesized and kindly provided to us by Dr. Kiyoshi Fujisawa (Tokyo Institute of Technology).

EPR Spectroscopy. EPR spectra were recorded at liquid helium temperatures on a Bruker 220-D SRC spectrometer, equipped with an Air Products Helitran liquid He cryostat. Temperatures were measured with a carbon glass resistor mounted in an EPR tube. Samples for EPR spectroscopy contained ∼2 mM Fe and 1 M Na_2SO_4 and were ∼50% (w/v) glycerol. Based on the EPR and rR spectra, the formation of dimers and the presence of intermolecular interactions were minimal under these conditions. The presence of glycerol significantly reduced the line width. The saturation behavior of the samples was determined at 4.5 K, and $P_{1/2}$ was found to be ∼45 mW. The spectra shown were recorded at 0.25 mW under nonsaturating conditions. EPR spectra were simulated with an updated version of the program EPR[23] employing methods similar to those described in the literature.[24]

Absorption Spectroscopy. Room-temperature absorption spectra were recorded on a Hewlett-Packard HP8452A diode-array spectrophotometer and a Cary 17 spectrophotometer. LT-ABS spectra were obtained at 14 K in the double-beam mode of the Cary 17 spectrophotometer by using a Janis Research Super Vari-Temp liquid helium cryostat.

MCD Spectroscopy. MCD spectra were collected on circular dichroism spectropolarimeters (Jasco 500, S1, and S20 PM tubes for the UV/vis/near-infrared (IR) regions and a J200, InSb detector for the near-IR region) with sample compartments modified to accommodate magnetocryostats (Oxford Instruments, SM4−7T). High-quality optical glasses were obtained by adding 50% (w/v) glycerol to the samples that were frozen in metallic sample compartments between two Infrasil quartz disks separated by a 3-mm Neoprene spacer. Experiments in the near-IR (700−2000 nm) were done with deuterated buffers (99.9 atom % D; Aldrich) and d_3-glycerol (98 atom % D; Aldrich). For VTVH-MCD spectroscopy, accurate temperatures were measured with a carbon glass resistor supported by a hole in the sample cell. $\Delta\epsilon$ values are quoted on a M^{-1} cm^{-1} T^{-1} basis by using the data obtained in the linear response regime ($\leq 2T$) with sample concentrations calibrated from room-temperature absorption spectra prior to freezing (using ϵ_{520} = 520 M^{-1} cm^{-1}). Iterative, simultaneous Gaussian fits to the LT-ABS and MCD spectra were carried out with the programs Origin 4.0 (Microcal Software) and Peak Fit 4 (AISN Software).

VTVH-MCD Analysis. VTVH-MCD data were analyzed with use of a theory and an associated fitting program that will be described in detail in a forthcoming paper.[25] Fits were based on the Levenberg−Marquad algorithm as implemented in the numerical recipes suite of programs[26] with derivatives evaluated by a straightforward finite-difference method.

rR Spectroscopy. rR spectra were obtained by using a series of lines of Kr^+ (Coherent 190C−K) and Ar^+ (Coherent Sabre 25/7) ion lasers with incident power in the 5−30 mW range and a backscattering geometry of ∼135°. The scattered light was dispersed by a triple monochromator (Spex 1877 CP, equipped with 1200, 1800, and 2400 groves/mm gratings) and detected with a back-illuminated charge-coupled device detector (Princeton Instruments, ST-135). Raman data were obtained for both liquid and frozen solution samples with use of NMR capillaries. In the latter case, a liquid nitrogen flow system was used to cool the samples to ∼170 K. Excitation profiles were obtained from three samples prepared under identical conditions with 1M Na_2SO_4 included as an internal standard (Na_2SO_4 was found to have no effect on the EPR spectra of the complex). A Raman spectrum of the Fe(III)−EDTA precursor in an identical tube, at the identical concentration, and measured under identical conditions was used to estimate the background. The Raman spectra for the excitation profile were obtained by first subtracting a smooth background (either linear or quadratic) from the data and then subtracting the unweighted Fe(III)−EDTA spectrum from that of the peroxide complex. Alternatively, spectra were background-corrected and resolved into Gaussian peaks to estimate the contribution of the peaks attributed to either the ν_{OO} or ν_{FeO} modes by using the software Peak Fit 4. Both methods led to similar results. Raman shifts were calibrated by using the Raman peaks of propionitrile as a standard.

Normal Coordinate Analysis (NCA). NCA calculations used the FG-matrix method of Wilson[27] and were based on a Urey−Bradley force field as implemented in a modified version of the Schachtschneider program.[28]

rR Profile Simulation. rR excitation profiles were simulated by using the time-dependent theory of electronic spectroscopy developed by Heller and co-workers[29a,b] and a script written for Mathcad 5.0 by Dr. Thomas Brunold.

DFT Calculations. These calculations were performed on an IBM 3BT-RS/6000 workstation, using the Amsterdam density functional (ADF) program version 2.0.1.[30] The local exchange-correlation approximation (LDA) of Vosko and co-workers[31] was used, together with the gradient corrections of Becke[32] for the exchange and of Perdew[33] for the correlation. All calculations were of the spin-polarized type. An uncontracted triple-ζ basis set (ADF basis set IV) with a single polarization function was used for all atoms. Core orbitals were frozen through 1s (N,O) and 3p (Fe).

(23) Neese, F. Quantum Chemistry Program Exchange; University of Indiana: Bloomington, IN, 1995; Bull. 15, p 5.

(24) Gaffney, B. J.; Silverstone, H. J. In *Biological Magnetic Resonance* Vol. 13 in *EMR of Paramagnetic Molecules*; Berliner, J.; Reuben, J., Eds.; Plenum Press: New York, 1993; pp 1−57.

(25) Neese, F.; Solomon, E. I. Manuscript submitted for publication.

(26) Press, W. H.; Teukolsky, S. A.; Vetterling, W. T.; Flannery, B. P. *Numerical Recipes in C*, 2nd ed.; Cambridge University Press: Cambridge, 1992.

(27) Wilson, E. B. Jr.; Decius, J. C.; Cross, P. C. *Molecular Vibrations*; Dover Publications: New York, 1955.

(28) (a) Schachtschneider, J. H. Techn. Rep. No. 57-65; Shell Development Co.: Emeryville, CA, 1966. (b) Fuhrer H.; Kartha, V. B.; Kidd, K. G.; Krueger, P. J.; Mantsch, H. H. *Computer Programs for Infrared Spectroscopy*; National Res. Council of Canada, 1976; Bull. 15.

(29) (a) Lee, S. Y.; Heller, E. J. *J. Chem. Phys.* **1979**, *71*, 4777. (b) Tannor, D. J.; Heller, E. J. *J. Chem. Phys.* **1982**, *77*, 202. (c) Myers, A. B.; Mathies, R. A. In *Biological Applications of Raman Spectroscopy*; Spiro, T. G., Ed.; Wiley: New York, 1987; Vol. 2, pp 1−58. (d) Zink, J. I.; Shin, K. S. K. *Adv. Photochem.* **1991**, *16*, 119.

(30) (a) Baerends, E. J.; Ellis, D. E.; Ros, P. *J. Chem. Phys.* **1973**, *2*, 42. (b) te Velde, G.; Baerends, E. J. *Int. J. Comput. Phys.* **1992**, *99*, 84.

(31) Vosko, S. H.; Wilk, L.; Nusair, M. *Can. J. Phys.* **1980**, *58*, 1200.

(32) Becke, A. D. *J. Chem. Phys.* **1986**, *84*, 4524.

(33) Perdew, J. P. *Phys. Rev. B.* **1986**, *33*, 8822.

Spin unrestricted B3LYP, BLYP, and Hartree−Fock calculations were carried out with the Gaussian 94 program suite.[34] The standard 6−31G basis set was used for all ligands and 6−311G for Fe. Natural populations analysis was done by the method of Weinhold and co-workers.[35]

INDO/S-CI Calculations. All semiempirical calculations reported were of the valence-only type and were carried out with the program Orca, developed by one of us (F.N.). The INDO/S model of Zerner and co-workers[36] was used, as were the valence shell ionization potentials and Slater−Condon parameters listed by Bacon and Zerner[36b] and the standard interaction factors $f_{P_\sigma P_\sigma} = 1.266$ and $f_{P_\pi P_\pi} = 0.585$. No change of semiempirical parameters was found necessary for the present study. Restricted open-shell (ROHF)[37] SCF calculations were tightly converged on the $^6A_1$ ground-state and this state served as reference for configuration interaction (CI) calculations. The CI matrix was formed by using a Rumer diagram algorithm.[38] Stable results for the sextet spin states were obtained by including all single excitations into the singly occupied MOs (SOMOs), and from the SOMOs into all virtual orbitals, together with the double excitations from the highest 14 doubly occupied MOs (DOMOs) into the SOMOs. This scheme leads to ∼300 configuration-state functions (CSFs) in each irrep of the C_{2v} point group. Larger active spaces do not change our conclusions (compare supporting information S6). Oscillator strengths were calculated in the dipole length formalism by including only one center contributions. The **D**-tensor was calculated from the sextet and quartet CI wave functions by using a recently developed theory.[39] The spin−orbit-coupling (SOC) constants used were $\zeta_{3d}(\mathrm{Fe}) = 430\ \mathrm{cm}^{-1}$, $\zeta_{2p}(\mathrm{N}) = 76\ \mathrm{cm}^{-1}$, and $\zeta_{2p}(\mathrm{O}) = 150\ \mathrm{cm}^{-1}$.[40] Cartesian coordinates of the models used in the calculations are included as Supporting Information (S1).

Results and Analysis

1. EPR. ZFS Analysis. EPR spectra obtained for the Fe(III)−EDTA−peroxide complex are presented in Figure 1A. They are dominated by an intense signal in the $g = 3-6$ region. Addition of ∼50% glycerol leads to the resolution of two weak features in the $g = 8-10$ region that were otherwise unresolved. The spectra are well understood in terms of the weak magnetic field limit[24,41] for an $S = {}^5/_2$ system and the standard spin Hamiltonian:[24,41]

$$H_{\mathrm{spin}} = \beta\vec{B}\mathbf{g}\vec{S} + D[S_z^2 - {}^1/_3S(S+1)] + E[S_x^2 - S_y^2] \quad (1)$$

where β is the Bohr magneton, $\vec{B}$ the magnetic flux density, $\mathbf{g}$ the electronic g-tensor, $\vec{S}$ the total spin of the ground state, and

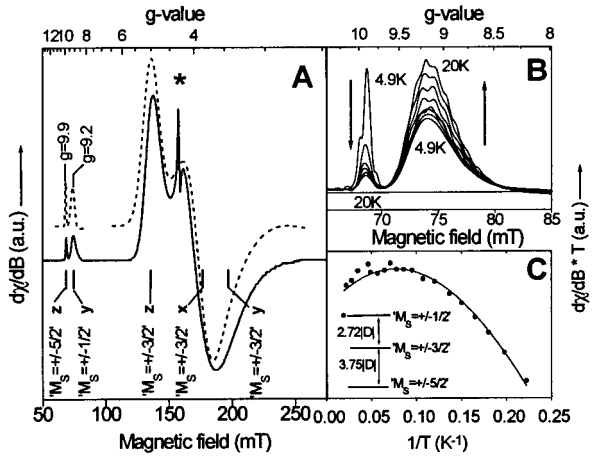

Figure 1. (A) (—) Low-temperature (4.9 K) X-band (9.5 GHz) EPR spectra of the Fe(III)−EDTA−peroxide complex at pH 11.5. The asterisk denotes a signal arising from a minor amount (≤1%) of unreacted Fe(III)−EDTA precursor. The bars denote the resonance positions predicted from the rhombogram method.[24,41] The attached label denotes the Kramers doublet and principal molecular orientation from which the transition arises. (- - -) Simulated spectra as described in the text by using line widths $W_{x,y,z} = 250, 230, 70$ MHz in the region $g = 8-10$ ($D = -1.2\ \mathrm{cm}^{-1}$) and $W_{x,y,z} = 551, 1000, 499$ MHz for $g = 3-6$. (B) Temperature dependence of the two low-field ($g = 8-10$) resonances between 4.9 and 20 K. (C) Boltzmann fit to Curie law−corrected data for the temperature dependence of the resonance arising from the middle Kramers doublet. The solid line is a least-squares fit to the data with $D = -0.77\ \mathrm{cm}^{-1}$.

D and E are the axial and rhombic ZFS parameters, respectively[41a] ($0 \le E/D \le {}^1/_3$).[42] Note that the form of eq 1 implies a choice of coordinate system, which will be discussed later in the paper. Usually for high-spin ferric complexes, $\mathbf{g} \approx g_0\mathbf{1}$, where $\mathbf{1}$ is the 3×3 unit matrix and g_0 is close to the free electron g-value ($g_e = 2.0023...$).[41a,43] For $D \gg h\nu$ (the energy of the microwave, ∼0.3 cm^{-1} at X-band), the three Kramers doublets of a $S = {}^5/_2$ system act approximately like independent "$S = {}^1/_2$" systems with effective g-values that are dependent only on E/D. From plots of the effective g-values versus E/D[24,41] we conclude that $E/D \approx 0.21$ for the Fe(III)−EDTA−peroxide complex at pH 11.5, consistent with an earlier study.[18c] According to this analysis, the dominant signal in the $g = 3-6$ region arises from the "$M_S = \pm{}^3/_2$", the feature at $g = 9.2$ from the "$M_S = \pm{}^1/_2$", and the resonance at $g = 9.9$ from the "$M_S = \pm{}^5/_2$" Kramers doublet (Figure 1). Control experiments show no comparable signals in the $g = 9-10$ region for the Fe(III)−EDTA precursor. The temperature dependence of these two signals at $g = 9.2$ and $g = 9.9$ (Figure 1B) is consistent only with the "$M_S = \pm{}^1/_2$" doublet being highest in energy in the peroxo complex; that is, D in eq 1 must be negative. A value for D of $-0.77\ \mathrm{cm}^{-1}$ is then obtained by a Boltzmann fit to the Curie law−corrected intensity of the strong signal in the $g = 3-6$ region (Figure 1C).

An independent estimate of the magnitude of D can be obtained from simulation of the EPR spectrum at a given temperature by use of an accurate solution of eq 1. D is obtained from the relative intensities of two peaks that originate from different Kramers doublets. The estimates obtained from the simulations are somewhat larger than those from the Boltzmann

(34) Frisch, M. J.; Trucks, G. W.; Schlegel, H. B.; Gill, P. M. W.; Johnson, B. G.; Robb, M. A.; Cheeseman, J. R.; Keith, T.; Petersson, G. A.; Montgomery, J. A.; Raghavachari, K.; Al-Laham, M. A.; Zakrzewski, V. G.; Ortiz, J. V.; Foresman, J. B.; Cioslowski, J.; Stefanov, B. B.; Nanayakkara, A.; Challacombe, M.; Peng, C. Y.; Ayala, P. Y.; Chen, W.; Wong, M. W.; Andres, J. L.; Replogle, E. S.; Gomperts, R.; Martin, R. L.; Fox, D. J.; Binkley, J. S.; Defrees, D. J.; Baker, J.; Stewart, J. P.; Head-Gordon, M.; Gonzalez, C.; Pople, J. A. *Gaussian 94*, Revision C.3; Gaussian, Inc.: Pittsburgh, PA, 1995.

(35) Glendening, E. D.; Reed, A. E.; Carpenter, J. E.; Weinhold, F. *NBO Version 3.1*, distributed with *Gaussian 94.*

(36) (a) Ridley, J.; Zerner, M. C. *Theor. Chim. Acta* **1973**, *32*, 111. (b) Bacon, A. D.; Zerner, M. C. *Theor. Chim. Acta* **1979**, *53*, 21. (c) Zerner, M. C.; Loew, G. H.; Kirchner, R. F.; Mueller-Westerhoff, U. T. *J. Am. Chem. Soc.* **1980**, *102*, 589. (d) Anderson, W. P.; Edwards, W. D.; Zerner, M. C. *Inorg. Chem.* **1986**, *25*, 2728.

(37) Edwards, W. D.; Zerner, M. C. *Theor. Chim. Acta* **1987**, *72*, 347.

(38) (a) Boys, S. F.; Reeves, C. M.; Shavitt, I. *Nature* **1956**, *178*, 1207. (b) Sutcliffe, B. T. *J. Chem. Phys.* **1966**, *42*, 235. (c) Cooper, I. L.; McWeeny, R. *J. Chem. Phys.* **1996**, *43*, 226. (d) Reeves, C. M. *Commun. ACM.* **1966**, *9*, 276. (e) Pauncz, R. *Spin Eigenfunctions. Construction and Use;* Plenum Press: New York, 1979.

(39) Neese, F.; Solomon, E. I. *Inorg. Chem.*, in press.

(40) Edlen, B. *Encyclopedia of Physics* 1964, 80.

(41) (a) Abragam, A.; Bleaney, B. *Electron Paramagnetic Resonance of Transition Ions*; Dover: New York, 1970. (b) Castner, T.; Newell, G. S.; Holton, W. C.; Slichter, J. P. *J. Chem. Phys.* **1960**, *32*, 668. (c) Eickman, H. H.; Klein, M. P.; Shirley, D. A. *J. Chem. Phys.* **1965**, *42*, 2113. (d) Aasa, R. *J. Chem. Phys.* **1970**, *52*, 3919.

(42) Blumberg, W. E. In *Magnetic Resonance in Biological Systems*; Ehrenberg, A.; Malmström, B. G., Eds.; Pergamon Press: Oxford, 1967; pp 110−133.

(43) The MO calculations described in part 5 of this paper predict *g*-values of 2.006, 2.011, and 2.013 for the Fe−EDTA−peroxide complex.

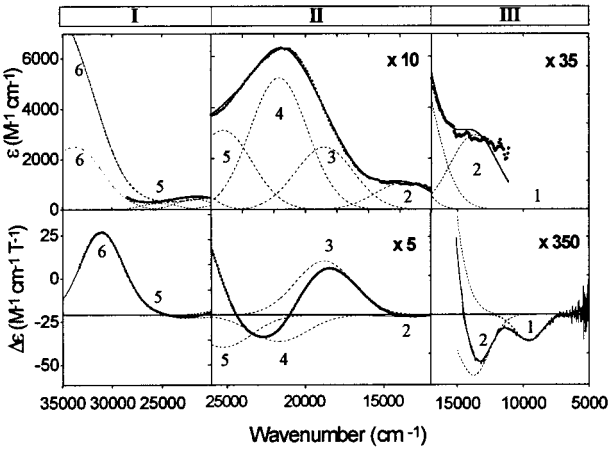

Figure 2. ABS (upper panel) and MCD (lower panel) data for the Fe(III)−EDTA−peroxide complex at pH 11.5. Gaussian curves (dotted lines) resulting from a simultaneous least-squares fit to both sets of data are shown, together with the numbering scheme used throughout the paper (parameters in Table 1). Bold dots are low-temperature (14 K ABS, 5 K MCD) experimental data and solid lines are the Gaussian fits. The absorption data for region I are from room-temperature measurements.

fit and are in the range $D \approx -1.0$ to -1.25 cm^{-1}. The signal at $g \approx 9.9$ arises from a formally $|\Delta M_S = 5|$ transition, and at $E/D \approx 0.21$ its transition intensity is predicted to be approximately an order of magnitude smaller than that of the formally $|\Delta M_S = 1|$ transition within the "$M_S = \pm^1/_2$" Kramers doublet.[24] However, for $D \approx -1.2$ cm^{-1} the Boltzmann population difference of the "$M_S = \pm^5/_2$" doublet at 5 K is ∼8-folder greater than that of the "$M_S = \pm^1/_2$" doublet, thus compensating for the lower transition probability. The strongly increased line widths of the transitions within the "$M_S = \pm^3/_2$" doublet are qualitatively understood from the fact that the slopes of the effective g-values as a function of E/D are much larger for these transitions than for those originating from the "$M_S = \pm^1/_2$" and "$M_S = \pm^5/_2$" doublets in the region of intermediate rhombicities.[24] No attempt was made to model an inhomogeneous E/D distribution ("E/D-strain"); therefore, the $g = 8-10$ and $g = 3-6$ regions were simulated independently in Figure 1 with $E/D = 0.21 \pm \sim 0.006$ but with different effective line widths. From the simulations, the Fe(III)−EDTA impurity signal accounts for ≤1% of the total double-integrated signal intensity.

Thus, the Fe(III)−EDTA−peroxide complex ($E/D \approx 0.21$) is more axial than its Fe(III)−EDTA precursor ($E/D \approx 0.33$)[41d] and $D = -1.0 \pm 0.25$ cm^{-1}.

2. ABS and Low-Temperature MCD (LT-MCD). Excited States. A. Visible Region (Region II). Upon addition of H_2O_2 to Fe(III)−EDTA at elevated pH, an absorption band at 520 nm (19 200 cm^{-1}, the "purple band") develops ($\epsilon_{520} = 520$ M^{-1} cm^{-1}), which has been ascribed to a peroxide-to-iron ligand-to-metal charge transfer (LMCT) transition.[16a,18a,b] Under the conditions chosen, this band titrates with an equilibrium binding constant of ∼1700 M^{-1}, somewhat lower than previously reported.[13,16] ABS data were obtained at room temperature (not shown) and at low temperature (14 K) on frozen-solution glass samples (Figure 2, upper panel). Solutions of the peroxo complex change their color from purple to orange on freezing, which has been attributed to a narrowing of the charge transfer (CT) band.[18b] However, the spectra in Figure 2 show only a limited narrowing; they shift by ∼3000 cm^{-1} to higher energy on freezing.[44] In the present study we focus on the low-temperature form and perform all the spectroscopy on the frozen state.[45] The low-temperature MCD spectra (Figure 2, lower panel) show that the CT band centered at 21 700 cm^{-1} is associated with at least two electronic transitions, as indicated by the derivative-shaped signal in the region 18 000−23 000 cm^{-1} (Figure 2). Their C/D ratios are <0.1 (Table 1) and therefore typical for CT transitions.[46] The simultaneous Gaussian fit of the LT-ABS and MCD data, however, requires a third band to be present under the envelope of the purple band, which is centered at 25 800 cm^{-1} (Figure 2, band 5). This band is refined as a negative MCD band. However, because of the extensive overlap with band 6, its precise MCD intensity is difficult to estimate.

Table 1. Fit Parameters for the Simultaneous Gaussian Resolution of the Low-Temperature (14 K) Absorption and MCD (5 K) Spectra Shown in Figure 2

band	energy (cm^{-1})	fwhm (cm^{-1})	ϵ_{max} (M^{-1} cm^{-1})	$\Delta\epsilon$ (M^{-1} cm^{-1} T^{-1})	f_{osc} × 10^4	$\bar{C}_0/\bar{D}_0$[f] × 10^3
1	9 540	2 590[a]	−	−0.066	−	−
2	13 740	2 820[a]	86[e]	−0.150	17	7
3	18 800	4 310	202	4.6	40	84
4	21 700	4 310	425	−2.9	84	25
5	25 250	4 310	257	−3.5[d]	51	104[d]
6	31 050	5 040[b]	[c]2500−6500	72	675−1750	41−107

[a] Measured from the MCD spectrum in deuterated solvent. [b] Measured from the uncorrected MCD spectrum. The Fe(III)−EDTA contribution in this spectral region is ≤10%. [c] Obtained from the room-temperature absorption spectrum; see text for a discussion of the uncertainty in this value. [d] Value uncertain because of extensive overlap with the very strong positive band 6. [e] Value is an upper limit, given the uncertainties in the baseline of the low-temperature absorption experiments. [f] $\bar{C}_0/\bar{D}_0 = (\Delta\epsilon/\epsilon_{max})(kT/\beta B)$, where T and B are the temperature and field of the MCD spectrum taken in a regime of B/T where the MCD response is linear.

B. Near-IR Region (Region III). MCD spectra in the near-IR region show two weak MCD bands at 9540 and 13 740 cm^{-1}, with no additional transitions down to 5000 cm^{-1}. Based on its energy, small bandwidth (Table 1), and low intensity, band 1 at 9540 cm^{-1} is assigned to the lowest-energy spin-forbidden $^6A_1 \rightarrow {}^4T_1$ ligand field transition. This transition, which is known to increase in energy with decreasing ligand field strength,[47] is found at 16 500−18 100 cm^{-1} in tetrahedral ferric complexes, at 7200−11 400 cm^{-1} in octahedral ferric complexes, and at intermediate energies for 5-coordinate geometries and is expected at lower energies for 7-coordinate complexes.[48] In the Fe(III)−EDTA−peroxo complex, the energy is typical for a distorted octahedral complex. The energy, bandwidth, and intensity of band 2 are consistent with an assignment to the second ligand field transition $^6A_1 \rightarrow {}^4T_2$, which usually falls in the 12 000−15 000 cm^{-1} range for distorted octahedral complexes. Both transitions are much more intense in the MCD spectrum than are the corresponding transitions of the Fe(III)−EDTA precursor, which could not be observed in the concentra-

(44) Similar spectral shifts have been observed for a related side-on manganese peroxo complex (Kitajima, N.; Komatsuzaki, H.; Hikichi, S.; Osawa, M.; Moro-oka, Y. *J. Am. Chem. Soc.* **1994**, *16*, 11596) and appear to be related to hydrogen bonding interactions with the bound peroxide that change on freezing. A similar situation might exist for η^2-Fe-EDTA-O$_2$. Especially the solvent-exposed π_v^* orbital is a prime candidate for such an interaction since the absorption intensity in the visible region mainly reflects the properties of this orbital (vide infra).

(45) From the relatively small shift of the O−O vibration on freezing (8 cm^{-1}, ref 18b), we may speculate that the conclusions carry over to the complex present in solution, with small modifications.

(46) Gewirth, A. A.; Solomon, E. I. *J. Am. Chem. Soc.* **1988**, *110*, 3811.

(47) Sugano, S.; Tanabe, Y.; Kamimura, H. *Multiplets of Transition Metal Ions in Crystals;* Academic Press: New York, 1970.

(48) (a) Kato, H.; Taniguchi, M.; Kato, T. *Chem. Phys. Lett.* **1972**, *14*, 231. (b) Holt, S.; Dingle, R. *Acta Chem. Scand.* **1968,** *22*, 1091. (c) Kato, H. *J. Chem. Phys.* **1973**, *59*, 1732. (d) Hatfield, W. E. *Inorg. Chem.* **1964**, *3*, 605. (e) Drummond, J.; Wood, J. S. *J. Chem. Soc., Chem. Commun.* **1969**, 1373.

tion range used in our experiments. This increased MCD intensity is consistent with a SOC mechanism that allows the formally spin-forbidden sextet−quartet transitions to gain electric dipole allowedness through mixing with electric dipole-allowed CT transitions. These are close in energy in the peroxo complex (starting at ~18 000 cm^{-1}) but are energetically far removed in the precursor (>35 000 cm^{-1}).[15b]

C. UV Region (Region I). As first anticipated by MO calculations and experimentally confirmed by rR spectroscopy (vide infra), additional iron−peroxide-related absorption intensity was expected in the 25 000−35 000 cm^{-1} region.[49] The MCD spectra show an intense positive band centered at 31 050 cm^{-1} (Figure 2, lower panel). The room temperature ϵ-value of the peroxo complex at 31 050 cm^{-1} is ~6500 M^{-1} cm^{-1}, consistent with the findings of McClune et al.[15] Subtraction of the spectrum of an equimolar solution of Fe(III)−EDTA results in a maximum centered at 33 500 cm^{-1} with $\epsilon \approx 2500$ M^{-1} cm^{-1} (Figure 2, upper panel). Thus, the peroxide contribution to the intensity is estimated to lie between these limits. The MCD intensity of Fe(III)−EDTA in the region of band 6 accounts for at most 10% of the total intensity. To have a *C/D* value ≤0.1 for this band, as is typical for CT transitions,[46] one might reasonably expect the absorption intensity to be on the upper end of the estimate in Table 1. One may also argue that the peroxide ligand is a stronger donor than any of the EDTA ligands and therefore the EDTA→Fe CT transitions are expected to move to higher energies in the peroxo complex, again supporting the higher-end estimate for the O_2^{2-} to Fe CT intensity.

3. VTVH MCD. Polarization. A. Data. Figure 3 presents MCD spectra collected at a series of different magnetic fields and temperatures. From their strong dependence on the measurement temperature, all observed spectral features are identified as MCD *C*-terms (Figure 3A). VTVH-MCD data were collected at the five peaks indicated by arrows in Figure 3A and the sets of data corresponding to bands 3, 4, and 6 are shown in Figure 3B. VTVH data collected at bands 1 and 2 are included as supporting information (S2). The data show a striking variation of magnetization behavior at different excitation wavelengths with respect to their nesting behavior and slope at high $\beta B/2kT$. Band 6 shows essentially no nesting and approaches a roughly constant value at $\beta B/2kT \approx 0.6$, whereas bands 3 and 4 both show a pronounced nesting and pass through a maximum around $\beta B/2kT \approx 0.3$, the maximum being more prominent for band 4.

B. Theory. Up to now, several methods have been reported to analyze nonlinear MCD behavior.[50] However, all of these methods depend on several assumptions about sublevel populations, transition polarizations, and axial symmetry of the magnetic coupling tensors. In a forthcoming publication we will present a theory that relates nonlinear MCD behavior to transition polarization and SOC for spin-allowed transitions ($S \geq {}^1/_2$) in low-symmetry molecular environments.[25] Problems involved in the analysis are (a) M_S is not a good quantum number for intermediate rhombicities and fields, and (b) crossings of the ground-state magnetic sublevels occur at magnetic fields of several tesla strength in the range of *D* that applies to the Fe(III)−EDTA−peroxide system. This means that a pertubation approximation to the ground-state magnetic

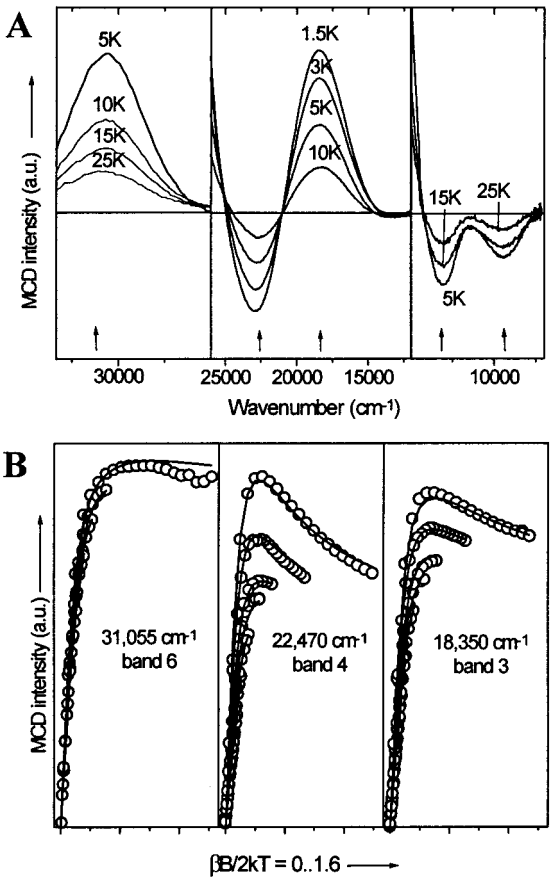

Figure 3. Variable-temperature−variable-field (VTVH) MCD data for the Fe(III)−EDTA−peroxide complex at pH 11.5. (A) Temperature dependence of the MCD spectrum at 2-T magnetic field. (B) VTVH data collected between 0 and 7 T and between 1.6 and 25 K at the energies indicated on the spectrum. Open circles = data; solid lines = fitted as described in the text.

eigenfunctions is not accurate enough. The present analysis is based on the following equation for the MCD *C*-term response of a spin-allowed transition (0→*J*) in a system with ground-state spin *S*:[25]

$$\bar{C}_0(0\rightarrow J) = \frac{\gamma}{S}\int\int\sum_i N_i(\langle S_x\rangle_i l_x M_{yz}^{\mathrm{eff}} + \langle S_y\rangle_i l_y M_{xz}^{\mathrm{eff}} + \langle S_z\rangle_i l_z M_{xy}^{\mathrm{eff}})\sin\theta d\theta d\phi \quad (2)$$

This equation follows from a more general expression if the chromophore symmetry is approximated to be orthorhombic.[25] In eq 2, γ is a collection of constants, N_i is the Boltzmann population of the *i*th magnetic ground-state sublevel, $\langle\vec{S}\rangle_i$ is its spin expectation value, $\vec{l}$ is a unit vector in field direction, θ and ϕ are the standard polar angles, and $\mathbf{M}^{\mathrm{eff}}$ is an effective transition moment product vector. Equation 2 shows that, to have a nonzero MCD *C*-term contribution, a ground-state magnetic sublevel must have a sufficiently high Boltzmann population, and the projections of the transition moment vectors onto the plane perpendicular to the magnetic field must be nonzero. In practice, N_i and $\langle\vec{S}\rangle_i$ are calculated from the diagonalization of eq 1, and eq 2 is numerically integrated to yield the total theoretical MCD intensity. This leaves the elements of $\gamma\mathbf{M}^{\mathrm{eff}}$ as the only fit parameters if the spin-Hamiltonian parameters are known. Test calculations reveal that eq 2 is insensitive to the value of *E/D* but is most sensitive to the sign of *D*.[25] For $D > 0$, a much more pronounced nesting is predicted than observed in Figure 3, thus confirming the EPR

(49) The band was previously observed in refs 15, 17, and 18 but was not attributed to a CT transition.

(50) (a) Schatz, P. N.; Mowery, R. L.; Krausz, E. R. *Mol. Phys.* **1978**, *35*, 1537. (b) Johnson, M. K.; Thomson, A. J. *Biochem. J.* **1980**, *191*, 411. (c) Bennet, D. E.; Johnson, M. K. *Biochim. Biophys. Acta* **1987**, *911*, 71. (d) Solomon, E. I.; Pavel, E. G.; Loeb, K. E.; Campochiaro, C. *Coord. Chem. Rev.* **1995**, *144*, 369. (e) Browett, W. R.; Fucaloro, A. F.; Morgan, T. V.; Stephens, P. J. *J. Am. Chem. Soc.* **1983**, *105*, 1868.

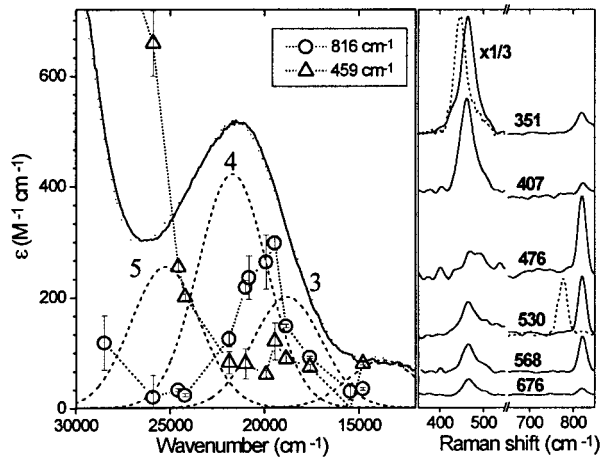

Figure 4. Resonance Raman (rR) data for the Fe(III)−EDTA−peroxide complex at pH 11.5 and ~170 K. Right panel: Background-corrected spectra obtained with the indicated laser excitation wavelengths (in nm). The dotted lines at 351 and 530 nm correspond to spectra taken on samples prepared with $H_2{}^{18}O_2$. Left panel: Excitation profiles for the 816 and 459 cm^{-1} vibrational modes, together with the Gaussian resolution of the low-temperature absorption spectrum from Figure 2.

result $D < 0$. For $D < 0$, eq 2 has a limited degree of sensitivity to $|D|$, mainly through the nesting behavior, whereas the effects of varying the polarizations are large.

C. Data Analysis. To limit the number of fit parameters, $E/D = 0.21$ and $D = -1.0$ cm^{-1} were fixed on the basis of the EPR results. Fits with $D = -1.2$ cm^{-1} are equally good, but much smaller or larger values of D result in significantly worse values for the goodness of the fit. Bands 6 and 3 were fitted by using eq 2 with two parameters $A_{\mathrm{satlim}} = \gamma M_{xy} = M_{\perp}$ and $M_{||} = M_{xz}/M_{xy} = M_{yz}/M_{xy}$. This approximation fails for band 4, which required all elements of $\gamma\mathbf{M}^{\mathrm{eff}}$ to be unequal. Note that the A_{satlim} parameter is determined by the arbitrary scaling of the isotherms. The fits in Figure 3 were obtained with $M_{||} = -0.026$ for band 3, $M_{||} = 0.226$ for band 6, and $M_{xz}/M_{xy} = 0.148$ and $M_{yz}/M_{xy} = -0.524$ for band 4. Thus all bands are predominantly x,y-polarized; there is little out-of-plane polarization for band 3, more for band 6, and the most prominent out-of-x,y-plane character is found for band 4. Note that the small value of $M_{||}$ for band 3 renders the fit insensitive to the individual values of M_{xz}/M_{xy} and M_{yz}/M_{xy}. Therefore, $M_{xz} \approx M_{yz}$ is not implied by the analysis. We emphasize that the coordinate system these polarizations refer to is the principal axis system of the ZFS-tensor **D**, which will be discussed below.

4. rR Spectra. A. Data. rR spectra were obtained with various laser excitation wavelengths for frozen solutions of the peroxo-complex (Figure 4). With 530 nm laser excitation, the most prominent feature is a relatively broad, resonance-enhanced vibrational mode at 824 cm^{-1} in solution. This was reported to shift to 815 cm^{-1} in the frozen state[18b] and was observed at 816 cm^{-1} in the present study. Based on its frequency, $^{16}O^{18}O$ isotope shift ($\Delta(H_2{}^{16}O_2/H_2{}^{16,18}O_2) = -21$ cm^{-1}),[18b] and profile behavior, this feature was assigned to the dominantly O−O stretching vibration.[18a,b] Data were also obtained for the $^{18}O^{18}O$ derivative and an isotope shift of −40 cm^{-1} was observed (530-nm trace in Figure 4, right; Table 2). In previous studies[18a,b] no metal−ligand vibration could be unambiguously identified, in part because of the weak enhancement of the features with visible laser irradiation and in part because of strong background signals from the quartz tubes and non-resonance enhanced metal−ligand vibrations in the 250−500 cm^{-1} region.[51] However, with excitation at 351 nm, a strongly resonance-enhanced vibration is observed at 459 cm^{-1} (Figure 4, right panel). This signal much exceeds the background and shifts to 446 cm^{-1} in samples prepared with $H_2{}^{18}O_2$. Based on its frequency, isotope shift, and profile behavior (vide infra), this vibrational mode is assigned to the predominantly Fe−O stretching vibration. This is the first reported observation of this mode for the Fe(III)−EDTA−peroxide complex and shows that the intense UV band (band 6) has significant peroxide-to-iron LMCT character.

Table 2. Calculated and Observed Vibrational Energies and Normal Coordinates for a Symmetric Side on Bound FeO_2 Model

	$^{16}O^{16}O$	$^{16}O^{18}O$[a]		$^{18}O^{18}O$	
	ν (cm^{-1})	ν (cm^{-1})	$\Delta\nu$ (cm^{-1})	ν (cm^{-1})	$\Delta\nu$ (cm^{-1})
Exp-ν_{OO}	816	795	−21	776	−40
NCA-ν_{OO}	820	798	−22	774	−46
Exp-ν_{FeO}	459	n.d.	n.d.	446	−13
NCA-ν_{FeO}	462	455	−7	445	−17
NCA-ν_{as}	421	408	−13	398	−23

	f[b]	% PED in ν_{OO}	% PED in ν_{FeO}	% PED in ν_{as}
O−O stretch	3.02	92.9	7.1	0
Fe−O stretch	1.55	7.1	92.9	100

(n.d. = not determined, PED = potential energy distribution, $\Delta\nu$ = isotope shift); Exp = determined experimentally. [a] Data from Ahmad et al.[18b] Note that the experimental ν_{OO} frequency of the $^{16}O^{18}O$ complex was shifted up by 1 cm^{-1} to reproduce the isotope shift reported by Ahmad et al.[18b] because in this study the ν_{OO} of the $^{16}O^{16}O$ complex was observed 1 cm^{-1} higher than in their study. [b] In mdyn Å^{-1}.

Scheme 2

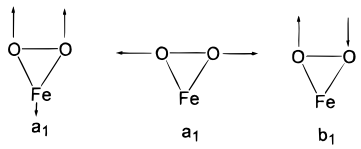

B. Normal Coordinate Analysis (NCA). Normal coordinate calculations were performed on a three-atom model for a side-on bound FeO_2 unit with C_{2v} symmetry. Such a model has three vibrational degrees of freedom (Scheme 2): two Raman active totally symmetric a_1 modes, which describe the Fe−O (ν_{FeO}) and O−O (ν_{OO}) stretches, respectively, and an antisymmetric combination of Fe−O stretches of b_1 symmetry (ν_{as}).

If a diagonal force field is assumed, the vibrational frequencies (in cm^{-1}) can be expressed in closed form as follows (see Supporting Information S3):

$$\nu_{as} = 1302.8\sqrt{f_{FeO}\left[\frac{1}{m_O} + \frac{1}{m_{Fe}}\left(\frac{R_{OO}^2}{2R_{FeO}^2}\right)\right]} \qquad (3a)$$

$$\nu_{FeO,OO} = 1302.8[{}^1/_2(f_{FeO}\mu_1 + f_{OO}\mu_2) \mp {}^1/_2\sqrt{(-f_{FeO}\mu_1 + f_{OO}\mu_2)^2 + 8f_{OO}f_{FeO}\mu_3^2}]^{1/2} \qquad (3b)$$

$$\mu_1 = \left[\frac{1}{m_O} + \frac{1}{m_{Fe}}\left(2 - \frac{R_{OO}^2}{2R_{FeO}^2}\right)\right] \mu_2 = \left[\frac{2}{m_O}\right] \mu_3 = \left[\frac{1}{m_O}\frac{R_{OO}}{2R_{FeO}}\right] \qquad (3c)$$

where m_{Fe} and m_O are the masses of the Fe and O atoms (in atomic units), R_{FeO} and R_{OO} are the interactomic distances (in Å), and f_{FeO} and f_{OO} are the force constants (in mdyn/Å). As is evident from eq 3, the vibrational frequencies are only weak

(51) Krishnan, K.; Plane, R. A. *J. Am. Chem. Soc.* **1968**, *90*, 3195.

functions of the geometrical parameters R_{FeO} and R_{OO} because $R_{OO}/R_{FeO} < 1$. Thus, the fact that these numbers are unknown does not affect the analysis to a significant extent. In the Supporting Information S3, we prove that the introduction of an off-diagonal force constant between the two Fe−O modes is equivalent to increasing f_{FeO} by the same amount. Thus it is not possible to improve the predicted isotope shifts by including this extra degree of freedom in the fit. An off-diagonal force constant between the O−O and the Fe−O stretch has a limited effect on the predicted isotope shifts of the two totally symmetric vibrational modes. Inclusion of this interaction (Supporting Information S3) leads to an estimate of this interaction force constant in the range −0.1 to 0.1 mdyn/Å and again does not affect the conclusions to a significant extent.

Table 2 lists the result of fitting the two force constants f_{FeO} and f_{OO} to five observed vibrational frequencies. The values were obtained with the reasonable estimates $R_{FeO} = 1.93$ Å and $R_{OO} = 1.41$ Å, consistent with the geometry assumed for the MO calculations (vide infra). The overall agreement between theory and experiment is reasonable for force constants of $f_{OO} = 3.02 \pm \sim 0.05$ mdyn/Å and $f_{FeO} = 1.55 \pm \approx 0.05$ mdyn/Å. The potential energy distribution in the two totally symmetric modes classifies the Fe−O and O−O stretching vibrations as modes with little mechanical coupling (Table 2).

C. Simulation of rR Profiles. Excited-State Distortions. Excitation profiles for the 459 and 816 cm^{-1} vibrational modes are also included in Figure 4. They demonstrate that excitation through bands 3 and 4 leads to dominant enhancement of ν_{OO} but also to a significant enhancement of ν_{FeO}. The striking effect is the very strong enhancement of the ν_{FeO} feature on excitation with UV radiation, which also leads to rapid photodecomposition of the complex. A three-point Shorygin plot[52] is consistent with the strong enhancement being a preresonance attributable to band 6 (not shown). Interestingly, excitation into band 5 does not lead to a strong O−O enhancement, despite the facts that the bandwidth of band 5 is comparable with those of bands 3 and 4 and that the maximum of the O−O enhancement does not coincide with the maxima of either band 3 or 4.

These experimental findings can be interpreted by simulating the resonance-enhancement patterns together with the ABS spectrum by using the time-dependent theory of electronic and rR spectroscopy developed by Heller and co-workers.[29a,b] This theory focuses on the time development of the nuclear wave function in the displaced excited-state potential and leads to the expression of the ABS spectrum in eq 4a:[29c]

$$I^{ABS}(E_L) \propto E_L \sum_J M_{0\rightarrow J}^2 \int_{-\infty}^{\infty} e^{it\{E_L - E^{(0)}_J\}/\hbar - \Gamma_J|t|/\hbar} \prod_p e^{-1/2(\Delta_p^J)^2\{1-\exp(-i\omega_p t)\}} dt \quad (4a)$$

where E_L is the energy of the incident radiation, $E_J^{(0)}$ is the energy of the zero phonon transition for excited state J, $\hbar\omega_p$ is the vibrational energy of the pth normal mode, $M_{0\rightarrow J}$ is the transition dipole moment for the $0\rightarrow J$ transition, and Γ_J describes the homogeneous line width of this transition.[53] In terms of the same quantities, the expression for the rR intensity of the fundamental ($0\rightarrow 1$ transition) in the kth normal mode is given by eq 4b:[29c]

$$I_k^{rR}(E_L) \propto E_L E_S^3 \left| \sum_J M_{0\rightarrow J}^4 \int_0^{\infty} e^{it\{E_L - E^{(0)}_J\}/\hbar - \Gamma_J|t|/\hbar} \left(\frac{1}{4}\Delta_k^J\right) \times (e^{i\omega_k t} - 1) \prod_p e^{-1/2(\Delta_p^J)^2\{1-\exp(-i\omega_p t)\}} dt \right|^2 \quad (4b)$$

where E_S is the energy of the scattered radiation. Among other approximations,[29c] it is assumed in eqs 4a and b that the nuclear motions in the ground and excited states are harmonic, described by the same normal coordinates (no Duschinsky rotation[29]), and that the force constants do not change in the excited states. The latter assumption is more critical, as will be discussed below. However, the simulations are expected to show only a limited sensitivity to variation in the force constants over a rather wide range and therefore the principal conclusions are unlikely to be strongly affected by these approximations.

D. Data Analysis. In the analysis, the dimensionless normal coordinate displacements and adiabatic excitation energies were varied to maximize agreement with the individual Gaussian distributions obtained from the analysis of the LT-ABS spectrum as well as the enhancement profiles for both totally symmetric modes. These are the only ones that can have $\Delta_p^J \neq 0$ and therefore rR intensity in the fundamental vibrational transition.[29,54] The relative band intensities were fixed to their values obtained from the analysis of the LT-ABS spectrum. The absolute signs of the normal coordinate displacements cannot be obtained from the simulation[29] and were chosen on the basis of chemical reasoning: A peroxide-to-iron CT transition from a peroxide π^*-orbital will strengthen the O−O bond. The Fe−O bond will be weakened in a transition where the donor MO has bonding and/or the acceptor MO has antibonding character with respect to the Fe−peroxide bond. Significant bonding interactions are required for CT intensity and thus it is expected that $\Delta_{OO} < 0$ and $\Delta_{FeO} > 0$ for all observed transitions. This choice is supported by the MO calculations described below. In this way the shape of the absorption band determines the absolute displacements, whereas the individual rR intensities determine the relative displacement along each distorting normal mode. Given the displacements, vibrational frequencies ($\nu_k = \omega_k/2\pi$), and mode descriptions from the NCA, the excited-state bond length changes are computed from eq 5.[29c]

$$\Delta R_i^J = 5.8065 \sum_k \frac{\Delta_k^J}{\sqrt{\nu_k}} L_{ik} \quad (5)$$

where L_{ik} is the ith element of the kth mass-weighted (normalized) eigenvector $\mathbf{L}_k$ for the kth normal mode and ΔR_i^J is the change in length (Å) along the ith internal coordinate in the Jth excited electronic state.

E. Fit Results. As shown in Figures 5A and 5B, the parameters collected in Table 3 lead to good agreement between theory and experiment for all absorption bands and for the two excitation profiles. The excited-state distortions determined from eq 5 for bands 3 and 4 are virtually identical and are reflected in their similar bandwidth (Table 3). For both bands, the excitation leads to an O−O bond length change of −0.12 Å (Scheme 3, Table 3). If an equilibrium bond length of 1.40−1.43 Å is assumed for the O−O bond, the excited-state bond length is 1.28−1.31 Å, close to the value found for superoxide

(52) Clark, R. H.; Mitchell, P. D. *J. Mol. Spectrosc.* **1974**, *51*, 458.

(53) S_p^J is the Huang−Rhys parameter corresponding to the pth normal mode in the Jth excited state and is related to the dimensionless displacement, Δ_p^J, along that mode by $S_p^J = {}^1/_2(\Delta_p^J)^2$.

(54) (a) Tang, J.; Albrecht, A. C. In *Raman Spectroscopy*; Szymanski, H. A., Ed.; Plenum: New York, 1970; Vol. 2; pp 33−68. (b) Hester, R. E. In: *Raman Spectroscopy*; Szymanski, H. A., Ed.; Plenum: New York, 1970; Vol. 2, p 101−138. (c) Clark, R. H. J.; Stewart, B. *Struct. Bonding* **1979**, *36*, 1.

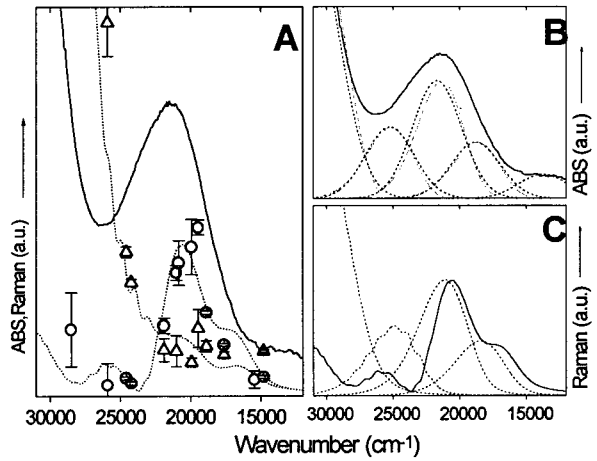

Figure 5. Simulation of ABS spectra and rR excitation profiles for the Fe(III)−EDTA−peroxide complex as described in the text. (A) (○) Experimental rR profile of the ν_{OO} feature at 816 cm^{-1}; (△) experimental rR profile of the ν_{FeO} feature at 459 cm^{-1}. Dotted lines are simulated profiles based on eq 4b. (B) Comparison of the Gaussian resolution of the LT-ABS spectrum (dashed lines) with the simulated absorption curves (dotted lines) based on eq 4a. (C) Resonance de-enhancement effects of the ν_{OO} feature at 816 cm^{-1}. Dotted lines are simulations of the individual excitation profiles under bands 2 to 6. The solid line is the final simulated profile, as in A.

Table 3. Dimensionless Normal Coordinate Displacement Parameters (Δ_{OO} and Δ_{FeO}) for the simulation of the rR excitation profiles and derived excited-state distortions (ΔR_{OO} and ΔR_{FeO})

band	Δ_{OO}	Δ_{FeO}	ΔR_{OO} (Å)	ΔR_{FeO} (Å)
3	−2.3	2.6	−0.12	+0.18
4	−2.3	2.6	−0.12	+0.18
5	−2.7	−0.9	−0.20	∼0
6	∼ −1	∼5	∼0	∼0.28

A homogeneous line width parameter $\Gamma = 500$ cm^{-1} was used for all bands. Normal coordinates used to calculate ΔR_{OO} and ΔR_{FeO} are from Table 2.

Scheme 3

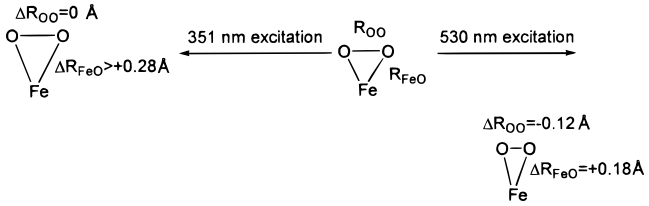

in ionic salts.[55] The two bands are therefore CT transitions of the type Fe(III)$O_2^{2-} \xrightarrow{h\nu}$ Fe(II)$O_2^{\bullet-}$ (Scheme 3, right).

The excited-state distortion parameters for band 6 are less certain, mainly due to the rapid photodecomposition of the complex but also to the uncertainties in the absolute contribution of the peroxide CT in the UV region. However, this band is at least 5−10-fold stronger than any of the bands of lower energy and therefore the distortion of the O−O bond is close to zero. In contrast, this band strongly activates the Fe−O bond, as reflected in a lower limit of +0.28 Å for the Fe−O distortion (Scheme 3 left), and must therefore be associated with an unusual peroxide-to-iron CT transition. For band 5, the simulations predict a sizable O−O distortion but little rR intensity. This can be understood from Figure 5C, which shows that the rR intensity of band 5 alone is much larger than when simulated in conjunction with bands 3, 4, and 6. Thus, the reason for the low ν_{OO} intensity for band 5 is a quantum mechanical interference effect that leads to resonance de-enhancement; this is also the cause of the shift in the maxima of the experimental profiles relative to the ABS bands (Figure 5C).

In summary, bands 3 through 5 are classified as CT transitions that give ferrous-superoxide-like excited states, whereas the strong band 6 behavior parallels that of μ:η^2:η^2 dicopper−peroxide complexes,[56,57] in that it leads to a strong activation of the metal−ligand bond and little distortion of the O−O bond. These findings can be understood through an examination of the specific bonding interactions that result from electronic structure calculations presented below.

5. Molecular Orbital Calculations. For the theoretical study we chose the ROHF−INDO/S-CI model of Zerner and coworkers,[36] because of its computational efficiency, ease of application to excited states, and well-documented success in this area.[36,58] The INDO/S results were complemented with DFT calculations, leading to a general picture emerging for the electronic structure of side-on bound iron−peroxide complexes that is reasonably consistent among the different theoretical methods and more importantly is also consistent with the experimental findings, as will be developed in detail below.

A. Estimate of Relevant Structure. Several possibilities exist for the structure of the Fe(III)−EDTA−peroxide complex: The peroxide ligand can bind in an end-on or a side-on fashion with different coordination numbers. To distinguish these posibilities, one may use the following available spectral information: (a) transition energies and intensities from ABS and MCD spectroscopy, (b) excited-state distortions and isotope shifts from rR spectroscopy, and (c) the negative sign of D from EPR spectroscopy. The most likely structure is identified by combining this set of information with the spectra and bonding descriptions obtained from MO calculations.

On a qualitative level, the bonding is dominated by the interactions of the peroxide π^* with the Fe-3d orbitals (vide infra) as shown in Scheme 4 for a 6-coordinate (6-c) side-on configuration (**1**), a 7-c side-on arrangement (**2**) and an end-on hydroperoxide (**3**).

From these orbital interactions, one expects a high-energy, high-intensity $\pi^*_\sigma \rightarrow$Fe-d$_\sigma$ transition for **1** because the relevant Fe-3d orbital is derived from the e$_g$ orbital set. These valence orbitals are defined below (Section 5.C). For **2**, one expects a low energy, high-intensity in the $\pi^*_\sigma \rightarrow$Fe-d$_\pi$ transition because the relevant Fe-3d orbital is derived from the t$_{2g}$ orbital set. For **3**, intense $\pi^*_\nu \rightarrow$Fe-d$_\pi$ and $\pi^*_\sigma \rightarrow$Fe-d$_\sigma$ transitions are anticipated. Figure 6 presents the spectra calculated for models **1** to **3** (Figure 6B−D) and compares them with the experimental spectrum (Figure 6A). Because the calculated spectra evidently follow the simple MO picture in Scheme 4, the best fit to the experimental spectrum is obtained by model **1**, the only one that correctly reproduces the intensity distribution and transition energies observed experimentally. For model **2** the calculated intensity pattern is a high-energy/low-intensity transition and a low-energy/high-intensity transition, which is the reverse of the

(55) Valentine, J. S. *Chem. Rev.* **1973**, *73*, 235. The free superoxide ion has a bond length of 1.33 Å (i.e., ref 20d).

(56) Solomon, E. I.; Tuczek, F.; Root, D. E.; Brown, C. A. *Chem. Rev.* **1994**, *94*, 827.

(57) (a) Ross, P. K.; Solomon, E. I. *J. Am. Chem. Soc.* **1991**, *113*, 3246. (b) Solomon, E. I.; Lowery, M. D. *Science* **1993**, *259*, 1575. (c) Tuczek, F.; Solomon, E. I. *Inorg. Chem.* **1993**, *32*, 2850.

(58) For review see (a) Zerner, M. C. In *Reviews in Computational Chemistry*; Lipkowitz, K. B.; Boyd, D. B., Eds.; VCH: Heidelberg, 1990; Vol. 2, pp 313−365. (b) Zerner, M. C. In *Metal−Ligand Interactions: From Atoms, to Clusters, to Surfaces*; Salahub, D. R.; Russo, N., Eds.; Kluwer Academic Publishers: Amsterdam, 1992; Vol. 2, pp 101−123. (c) Zerner, M. C. In *Metal Ligand Interactions*; Russo, N.; Salahub, D. R., Eds.; Kluwer Academic Publishers: Amsterdam, 1996; pp 493−531.

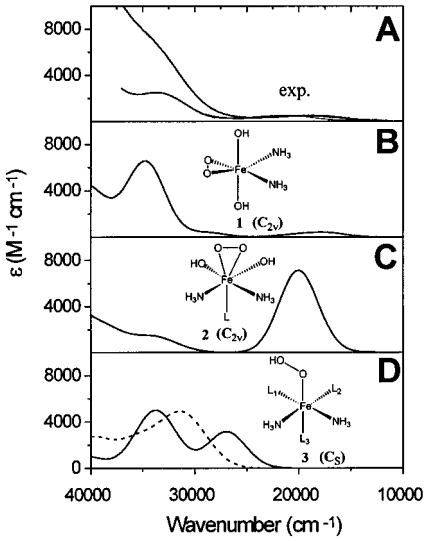

Figure 6. Comparison of the experimental ABS spectrum with calculated spectra for possible models for the Fe−EDTA−O_2 complex. All spectra were calculated with ROHF−INDO/S−CIS(D) method for 1000−1200 singly and doubly excited configurations. (A) Experimental room-temperature spectrum with two possible background subtractions as discussed in the text. (B) Calculated spectrum for a 6-c side-on model (**1**). (C) Calculated spectrum for a 7-c side-on model (**2**). (D) Calculated spectra for two end-on hydroperoxide models [$Fe(NH_3)_3(OH)_2(OOH)$] (**3**): solid line, axial OH^-; broken line, axial NH_3.

Scheme 4

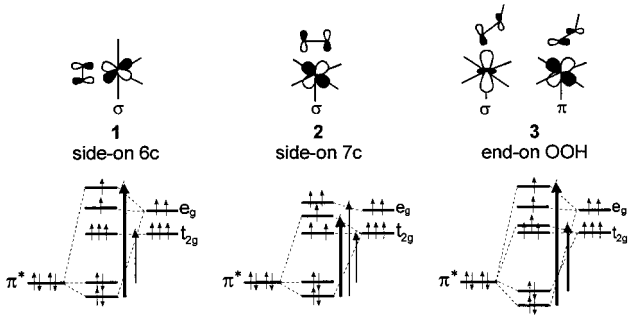

pattern observed experimentally. For model **3** the calculated intensity in the 15 000−25 000 cm^{-1} region is higher than observed experimentally because of the increased π-interactions depicted in Scheme 4. No high-spin end-on bound Fe(III)−OOH complex has yet been reported that could serve as a calibration for the calculations on model **3**. However, calculations on a model for a recently reported high-spin Fe(III)−alkylperoxide complex with a pure N-based coordination environment[59] and a putative low-spin Fe(III)−hydroperoxide complex[60] match the features of the published ABS spectra well.[61]

Additional evidence for a side-on coordination geometry comes from resonance Raman spectroscopy. The absence of an isotope splitting in the rR spectra of the mixed-isotope derivative $^{16}O^{18}O$ has strongly favored a side-on structure.[18b] However, if such a splitting were small,[62] it would not be resolved, given the rather large width of the ν_{OO} feature (fwhm $\approx 24\ cm^{-1}$), (b) the lack of an shift on the ν_{OO} feature on H_2O/D_2O replacement is rather strong evidence for a side-on structure relative to the alternative of an end-on hydroperoxide complex. Such a shift (4 cm^{-1}) has been observed for the hydroperoxide in oxyhemerythrin[63] and also for free hydrogen peroxide under the experimental conditions of Ahmad et al.[18b,64,65]

Finally, both **1** and **2** have substantially negative calculated values for D ($D \approx -1$ to $-2\ cm^{-1}$), whereas all models of type **3** that we have investigated theoretically[66] display calculated values for D that are either positive or slightly negative. This is a result of specific orbital interactions that will be analyzed later (Section 5.D).

In summary, strong experimental and theoretical evidence support a side-on structure in the Fe(III)−EDTA−peroxide complex, and the spectroscopic properties of such a complex are most easily matched with the 6-c model **1**. A 6-c geometry is also favored by the energy of the first observed spin-forbidden ligand field band (described in Section 2) and by the calculations. We therefore examine the electronic properties of **1** below.

Table 4. Comparison of Population Analysis for **1**[a]

method	Q_{Fe}	ρ_{Fe}	$Q_{peroxide}$	$\rho_{peroxide}$
B3LYP	1.52	4.00	−1.08	0.65
	(1.73)	(3.98)	(−1.19)	(0.66)
BLYP	1.37	3.83	−0.98	0.71
	(1.57)	(3.78)	(1.09)	(0.74)
UHF	2.07	4.51	−1.42	0.37
	(2.27)	(4.52)	(−1.53)	(0.36)
INDO/S	1.41	4.29	−1.23	0.49

[a] Numbers in parentheses were obtained from a natural population analysis. See Materials and Methods for details. Q = charge, ρ = spin density.

B. MO Diagram and Populations. The calculated MO diagram with sketches of selected MOs is presented in Figure 7[67] and contour plots of these MOs are shown in Figure 8. Consistent with the experimental description of the Fe−EDTA−peroxide complex as high-spin Fe(III)−O_2^{2-}, the calculations show the five singly occupied MOs to be of mainly Fe-3d character. However, as indicated by the population analysis (Table 4), the covalency of the Fe-peroxide bond is rather high. Depending on the method of calculation, the spin density on the peroxide ligand is between 0.35 and 0.75 electrons (Table 4).[68] Typically Hartree−Fock calculations on transition metal complexes give descriptions that are too ionic, whereas pure density functionals tend to overestimate the covalency of metal−ligand bonds.[69] Often the most accurate methods are hybrid density functional methods, with B3LYP being successfully tested for iron compounds.[70] In the present case the INDO/S results are close enough to those obtained from B3LYP (Table 4) to justify the use of this approximate method in the analysis of the bonding and excited states.

(59) (a) Zang, Y.; Elgren, T. E.; Dong, Y.; Que, L. Jr. *J. Am. Chem. Soc.* **1993**, *115*, 811. (b) Kim, J.; Larka, E.; Wilkinson, E. C.; Que, L. Jr. *Angew. Chem., Int. Ed. Engl.* **1995**, *34*, 2048. (c) Zang, Y.; Kim, J.; Dong, Y.; Wilkinson, E. C.; Appelman, E. H.; Que, L. Jr. *J. Am. Chem. Soc.* **1997**, *119*, 4197.

(60) Kim, C.; Chen, K.; Kim, J.; Que, L. Jr. *J. Am. Chem. Soc.* **1997**, *119*, 5964.

(61) Neese, F., Solomon, E. I. Unpublished results.

(62) Our NCA calculations on end-on bound peroxide and hydroperoxide complexes gave splittings in the range 0−10 cm^{-1} depending on the assumed geometry and force constants.

(63) Loehr, T. M. In *Oxygen Complexes and Oxygen Activation by Transition Metals*; Martell, A. E.; Sawyer, D. T., Eds.; Plenum Press: New York, 1988; pp 17−32.

(64) Root, D. E. Ph.D. Thesis, University of Stanford: Stanford, California, 1997.

(65) Preliminary normal coordinate calculations on an end-on FeOOH species—given the experimental vibrational frequencies, force field parameters close to those in ref 64, and a quantum mechanically optimized structure—predict that a deuterium shift would have been observable given the experimental bandwidth of the ν_{OO} feature.

(66) A variety of six-coordinate Fe−OOH models were investigated where the ligand set changed from pure N coordination (represented by NH_3) to mixed N, O coordination (O-ligands represented by OH^-). The geometry the Fe−O−O−H dihedral angle was varied. The O−O bond length, Fe−O bond length, and Fe−O−O angle were fixed to 1.41 Å, 1.9 Å, and 120°, respectively, with the last value resulting from an energy minimization using the ADF program, as described in *Materials and Methods*.

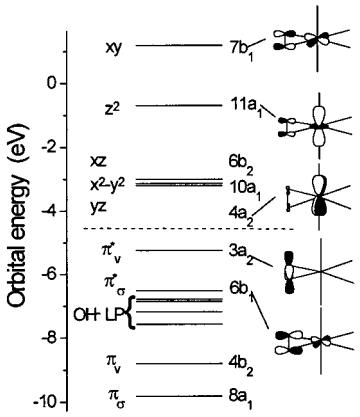

Figure 7. MO scheme for model **1** from ROHF−INDO/S calculations.[68] Levels below the horizontal line are doubly occupied, those above are singly occupied.

C. Nature of Bonding Interactions. As shown by the calculations and also observed in other metal−peroxide systems, the bonding between the iron and the peroxide is dominated by the Fe-3d and peroxide π* fragment orbitals (FMOS).[56] An octahedral field will split the five Fe-3d orbitals into a σ-antibonding set of e_g symmetry and a π-antibonding set of t_{2g} symmetry, separated by the energy 10 Dq. However, the highest effective symmetry that can be assumed for a side-on bound $FeL_2L_2'O_2$ complex is C_{2v}, as in **1** = $[Fe(OH)_2(NH_3)_2O_2]^{-}$), and therefore additional orbital splittings are observed (Figure 7). We have chosen a coordinate system where the *z*-axis is perpendicular to the FeO_2 plane and the *x*-axis points from Fe to the midpoint of the O−O bond (vide infra). Here the e_g set comprises the Fe-3d_{z^2} and 3d_{xy} orbitals transforming as a_1 and b_1, respectively. The t_{2g} set contains the Fe-3d_{xz}, 3d_{yz}, and 3$d_{x^2-y^2}$ orbitals transforming as b_2, a_2, and a_1 respectively. The peroxide π*-FMOs transform as b_1 and a_2 and are denoted π_σ^* and π_ν^*, corresponding to their orientation relative to the Fe−O_2 bond direction.[56] The corresponding peroxide-bonding π_σ^b and π_ν^b-orbitals transform as a_1 and b_1, respectively.

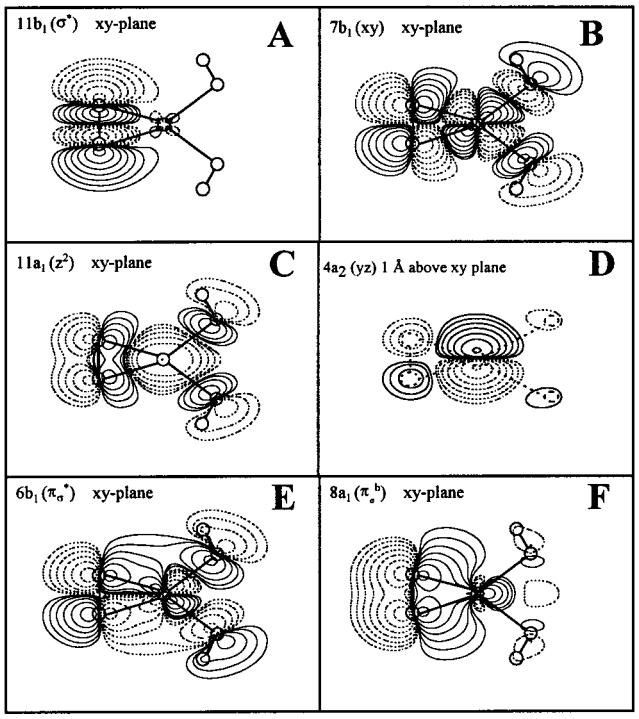

Figure 8. Contour plots of selected valence MOs for **1** from ROHF−INDO/S calculations. Contours were drawn at ±0.005, ±0.01, ±0.02, ... (electrons/bohr^3)$^{1/2}$.

As shown by the MO compositions in Table 5, the main bonding interaction occurs between the Fe-3d_{xy} and π_σ^*-FMOs, resulting in a strongly antibonding MO (7b_1(*xy*), Figure 8B). The corresponding bonding character is distributed over the MOs 5b_1 and 6b_1 (Figure 8E) because of mixing of the π_σ^*-FMO with a close-lying OH^- lone pair (Table 5, Figure 7). To simplify the discussion we will refer to the combination $2^{-1/2}$(5b_1 + 6b_1) as 6b_1'(π_σ^*). The strong Fe−peroxide σ-bonding interaction also leads to the large splitting of the 7b_1(*xy*) and 11a_1(z^2) orbitals observed in Figure 7. By contrast, interactions of the peroxide ligand with the iron t_{2g}-derived MOs (4a_2, 10a_1, and 6b_2) are weak, as indicated by the low-peroxide character in these MOs (Table 5) and their small energy-splitting (Figure 7), which is attributed to poor overlap (Figure 8D).

In addition to the strong σ-bond formed between Fe-3d_{xy} and the peroxide π_σ^*-FMO, another important interaction is apparent in Figure 8C. It involves the Fe-d_{z^2} MO and the bonding π_σ^b-FMO of the peroxide ligand and shows that the Fe-3d orbitals are energetically much closer to the doubly occupied ligand donor orbitals than to the empty peroxide σ*-FMO. A symmetry allowed interaction between the peroxide σ*-FMO and the Fe-3d_{xy} orbital would be interesting in relation to μ:η^2:η^2 peroxide−dicopper complexes.[56,57] Such an interaction represents back-bonding and greatly contributes to the weakening of the O−O bond in oxyhemocyanin and related μ:η^2:η^2 dicopper−oxygen complexes, that are known to exist in side-on peroxide and bis-μ-oxo forms.[71] However, in the present case there is no back-bonding interaction between Fe and peroxide in the side-on bound Fe(III)−peroxide complex, and

(67) In Figure 7 the ROHF−SCF method was used, which solves two sets of equations for the closed and open-shell MOs, respectively.[37] Because this method uses a realistic exchange potential for all electrons, the calculations show a feature that is typical for calculations on high-spin d^5 systems, namely, a large exchange stabilization of the singly occupied Fe-3d−based MOs below the highest occupied ligand−based MOs, even after correcting the ROHF orbital energies to conform to Koopmans theorem.[37] Despite this, the total molecular energy is lowest for the state in which the Fe-3d−based MOs are singly occupied. To more directly match the SCF to the CI results, the open-shell MOs have been shifted by 6.7 eV in Figure 7 so that the energy difference between the highest doubly occupied MO (3a_2(π_ν^*)) and the lowest iron-based MO (4a_2(yz)) roughly corresponds to the first observed CT energy. The simultaneous breakdown of the Aufbau principle and Koopmans theorem is typical for calculations on transition metal complexes, and a significant amount of CI is needed to obtain the proper ordering of states. In the present case we found it necessary to include double excitations of the form $\pi_\sigma^*,\pi_\nu^* \rightarrow$Fe-$d_i$, Fe-$d_j$ ($i \neq j$) to account for the electronic relaxation in the excited states. However, the main deviation from a single-particle picture is the reversed order of the $^6A_2^c$(3a_2(π_ν^*)→11a_1(z^2)) and $^6B_1^b$(3a_2(π_ν^*)→7b_1(xy)) states (Table 8). ΔCI calculations (not shown) predict the first vertical ionization to come from 7b_1 (≈2.5 eV for the naked ion) and a large electronic reorganization for any subsequent ionization.

(68) The spin densities are dominated from the contributions of the rather compact Fe-3d orbitals. They reflect the relevant donor properties more directly and are not as sensitive to the method of population analysis used as are the computed atomic charges.

(69) The prototypical molecule is $CuCl_4^{2-}$. Most pure-density functional methods behave similar to the X_α-SW method, which is known to overestimate covalency when Norman radii are used. See Solomon, E. I.; Baldwin, M. J.; Lowery, M. D. *Chem. Rev.* **1992**, *92*, 521, and references therein.

(70) (a) Ricca, A.; Bauschlicher, C. W. *Theor. Chim. Acta* **1995**, *92*, 123. (b) Glukhotsev, M. N.; Bach, R. D.; Nagel, C. J. *J. Phys. Chem. A* **1997**, *101*, 316. (c) Siegbahn, P. E. M.; Crabtree, R. H. *J. Am. Chem. Soc.* **1997**, *119*, 3103.

(71) (a) Halfen, J. A.; Mahapatra, S.; Wilkinson, E. C.; Kaderli, S.; Young, V. G.; Que, L. Jr.; Zuberbühler, A. D.; Tolman, W. B. *Science* **1996**, *271*, 1397. (b) Mahadevan, V.; Hou, Z. G.; Cole, A. P.; Root, D. E.; Lal, T. K.; Solomon, E. I.; Stack, T. D. P. *J. Am. Chem. Soc.* **1197**, *119*, 11996.

Table 5. MO Compositions Obtained for Selected Valence Orbitals of **1** in the electronic ground-state $^6A_1$ by ROHF-INDO/S calculations

				iron		peroxide		other ligands	
MO	label	ϵ (eV)	occ.[a]	%Fe-d	main-AO	$\%O_2$	main-FMO	$\%NH_3$	$\%OH^-$
$11b_1$	σ^*	13.0	0	0.1	-	99.9	σ^*	0	0
$7b_1$	xy	−5.50	1	60	$3d_{xy}$	34	π^*_σ	6	0
$11a_1$	z^2	−7.39	1	83	$3d_{z^2}$	5	π^b_σ	3	9
$6b_2$	xz	−9.70	1	96	$3d_{xz}$	2	π^b_ν	0	2
$10a_1$	x^2-y^2	−9.83	1	98	$3d_{x^2-y^2}$	1	π^b_σ	1	0
$4a_2$	yz	−9.90	1	96	$3d_{yz}$	1	π^*_ν	0	3
$3a_2$	π^*_ν	−5.25	2	0	$3d_{yz}$	96	π^*_ν	0	4
$6b_1$	$\pi^{*\,b}_{\sigma b}$	−6.51	2	10	$3d_{xy}$	22	π^*_σ	5	63
$5b_1$	$\pi^{*\,b}_{\sigma a}$	−7.57	2	26	$3d_{xy}$	40	π^*_σ	0	34
$4b_2$	π^b_ν	−8.80	2	3	$3d_{xz}$	80	π^b_ν	0	16
$8a_1$	π^b_σ	−9.82	2	13	$3d_{z^2}+4s-4p_x$	84	π^b_σ	0	3

[a] Note that the orbital energies for the open-shell orbitals (occ = 1) do not obey Koopman's theorem. [b] In the text we have taken the combination $2^{-1/2}(5b_1 + 6b_1)$ and refer to it as $6b_1'(\pi^*_\sigma)$ to simplify the discussion.

the σ^*-MO is virtually pure (Figure 8A, Table 5). This finding is consistent with the vibrational data, which show that the force constant of the O−O stretching vibration ($f_{OO} = 3.02 \pm 0.05$ mdyn/Å; see Section 4) is significantly higher than $f_{OO} = 2.4$ mdyn/Å found for oxyhemocyanin but similar to the recent determination of $f_{OO} = 3.1$ mdyn/Å in a cis-μ-1,2-peroxo-bridged diiron(III) complex,[72] where back-bonding is not present. The reasons for the lack of interaction of the Fe-3d orbitals with the peroxide σ^*-orbital are the high effective nuclear charge of trivalent iron[73] together with the substantial exchange stabilization of the high-spin d^5-configuration.[74] In addition, the charge donation from O_2^{2-} to the metal is less pronounced in the η^2-FeO_2 monomer than in the μ:η^2:η^2 peroxide−dicopper systems; therefore, the peroxide orbitals are less stabilized in the former (see *Discussion*).

These key findings from the theoretical study are emphasized in Figure 9, where the left side shows the Fe−O_2 fragment−fragment overlap. The diagram shows that the dominant interaction of the Fe-3d with the peroxide orbitals involves the peroxide π^*_σ- and Fe-$3d_{xy}$-FMOs, and that the interaction with the peroxide π^b_σ-FMO contributes significant bonding character to the $8a_1$-MO and also antibonding character to the $10a_1(x^2-y^2)$ and $11a_1(z^2)$ MOs. However, there is not much bonding character in the $3a_2(\pi^*_\nu)$-MO and also not much antibonding character in the singly occupied $4a_2(yz)$ MO, showing that only small π-interactions are involved in the bonding. Additional bonding character arises from the diffuse Fe-4s,p orbitals that are unoccupied and have small admixtures with the lower-lying valence MOs.

The upper panel on the right-hand side of Figure 9 shows the MOs evaluated along the O−O bond direction. The most striking feature is the almost equal O−O antibonding character contained in the $6b_1'(\pi^*_\sigma)$ and $7b_1(xy)$ MOs, which reflects the high covalency of the Fe−O bond. Since the $7b_1(xy)$ MO is

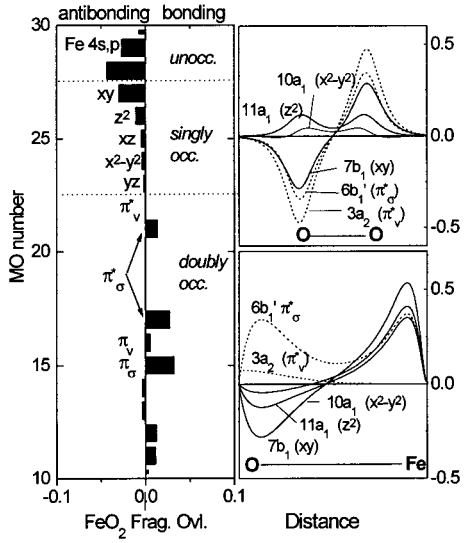

Figure 9. Analysis of bonding interactions for selected valence orbitals for **1** from the ROHF−INDO/S wave function. The left panel shows the Fe−O_2 fragment−fragment overlap in the valence region. The right-hand panels show selected MOs evaluated along the O−O (top) and Fe−O (bottom) bond directions [in $(\text{electrons/bohr}^3)^{1/2}$].

singly occupied, this covalent interaction contributes to a strengthening of the O−O bond relative to the free O_2^{2-} ion. Note that even minor admixtures of the peroxide σ^*-FMO into the valence b_1 MOs would have been detected in these plots, but they are not present—which emphasizes the lack of a back-bonding interaction. Both the $10a_1(x^2-y^2)$ and $11a_1(z^2)$ MOs show some O−O bonding character that is induced by the interaction with the O−O π^b_σ-FMO. As both of these MOs are half-occupied, this contributes to a weakening of the O−O bond relative to the free O_2^{2-} -ion and partially counteracts the effect of the Fe-$3d_{xy}$/peroxide-π^*_σ donor interaction. The $3a_2(\pi^*_\nu)$-MO is an almost pure peroxide π^*-orbital (Table 5) and therefore presents stronger antibonding with respect to the O−O bond than does $6b_1'(\pi^*_\sigma)$, again indicating weak π-interactions with the iron.

The lower panel on the right-hand side of Figure 9 shows the MOs evaluated and the Fe−O bond direction. As is apparent, the $6b_1'(\pi^*_\sigma)$ is the most-bonding and the $7b_1(xy)$ MO the most-antibonding orbital. Thus the main source of stability of the Fe−O bond is the σ-interaction between Fe-$3d_{xy}$ and the peroxide π^*_σ-MO. Again, significant antibonding character is

(72) Brunold, T. C.; Tamura, N.; Kitajima, N.; Moro-oka, Y.; Solomon, E. I. *J. Am. Chem. Soc.* **1998**, *120*, 5674.

(73) Copper has the highest electronegativity of the first-row transition metals. From a comparison of Cl K-edge X-ray absorption experiments for a series of metal−tetrachloride systems, it was deduced that the effective d-orbital energy is lowest and covalency highest for Cu among the divalent first-row transition metals. Fe(III) has a slightly higher effective charge and therefore also higher covalency than Cu(II). Thus the higher electronegativity of Cu(II) compensates much of the formally higher oxidation state for Fe(III). See Shadle, S. E.; Hedman, B.; Hodgson, K. O.; Solomon, E. I. *J. Am. Chem. Soc.* **1995**, *117*, 2259.

(74) (a) Butcher, K. D.; Gebhard, M. S.; Solomon, E. I. *Inorg. Chem.* **1990**, *29*, 2067. (b) Norman, J. G.; Jaeckels, S. C. *J. Am. Chem. Soc.* **1975**, *97*, 3833. (c) Norman, J. G.; Ryan, P. B.; Noodleman, L. *J. Am. Chem. Soc.* **1980**, *102*, 4279.

Table 6. Schematic Contributions to the ZFS of Side-on vs End-on Models

	source	side-on	end-on
$^4T_1$[a]	geometry	positive	negative
	covalency	negative	positive
$^4T_1$[c]	geometry	negative	positive
	covalency	negative	positive
$^6\Gamma$-CT	covalency	negative	small (positive)

Scheme 5

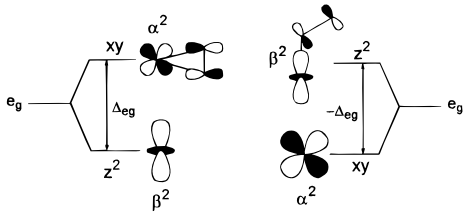

apparent in the $10a_1(x^2-y^2)$ and $11a_1(z^2)$ MOs, and the contribution of $3a_2(\pi_v^*)$-MO to the stability of the Fe−O bond is negligible.

To summarize, the bonding between peroxide and iron in the side-on geometry is dominated by a strongly covalent σ-bond formed between the peroxide π_σ^* and Fe-3d$_{xy}$ orbitals. There is no back-bonding interaction with the peroxide σ^*-FMO, but some σ-donor interaction between the O−O-bonding π_σ^b-FMO and the Fe-3d$_{z^2}$/Fe-3d$_{x^2-y^2}$ orbitals. The spectroscopic data can now be given a concise interpretation based on this bonding description.

D. Origin of ZFS. For a cubic high-spin d^5 complex, *D* and *E* in eq 1 are zero because the *x*, *y*, and *z* directions are equivalent and the ZFS is due to a difference in orbital angular momentum along the principal directions of **D**, which is induced by spin−orbit coupling of the $^6A_1$ ground-state with excited quartet-LF and sextet-CT states.[75] We have recently developed a theory that allows computation of the **D**-tensor from the full set of SCF-MO−CI wave functions.[39] The calculated value for **1** is -1.16 cm^{-1}, close to the lower end of the experimental estimate from EPR spectroscopy ($D = -1.0 \pm 0.25$ cm^{-1}). The calculated value for *E/D* is 0.18, again close to the value 0.21 observed experimentally. Importantly, the calculations define the principal axis system of the **D**-tensor as the one utilized in the symmetry designation in Section 5; that is, its *z*-axis is perpendicular to the FeO_2 plane and its *x*-axis points from the iron to the midpoint of the O−O bond (inset of Figure 10). This information is essential for the interpretation of the VTVH-MCD results (vide infra).

Insight into the bonding origin of the ZFS is obtained from a simplified model in which the dominant contributions to *D* arise from the low-symmetry energy-split components of the octahedral $^4T_{1g}$-LF states and from low-lying sextet-CT states. The small splittings and differences in covalency among the t_{2g}-derived orbitals are neglected in this model (compare Table 5). As explained in detail elsewhere,[39,75] there are two important contributions from the quartet states $^4T_{1g}^{a,c}$-LF, which to a good approximation can be broken down into contributions from anisotropic covalency and those from geometrical distortion-induced energy splittings (Table 6, Scheme 5) as in eq 6:

$$D(^4T_{1g}^{a,c}) = \frac{3}{320}\frac{\zeta_{Fe}^2}{\Delta_{O_h}}\gamma^2\left[4(5\alpha+3\beta)(\alpha-\beta) \pm \frac{\Delta_{e_g}}{\Delta_{O_h}}(11\alpha^2 + 2\alpha\beta + 3\beta^2)\right] \quad (6)$$

where ζ_{Fe} is the one-electron SOC constant for Fe ($\sim$430 cm^{-1}), Δ_{O_h} is the energy of the relevant $^4T_{1g}$ state in cubic symmetry, Δ_{e_g} is the one-electron energy difference between the $7b_1(xy)$ and $11a_1(z^2)$ orbitals, α^2 is the metal character in $7b_1(xy)$, β^2 is that in $11a_1(z^2)$, and γ^2 is the average metal character in the t_{2g}-derived MOs $4a_2(yz)$, $7b_2(xz)$, and $10a_1(x^2-y^2)$ (Table 5 and Scheme 5, left). The first term in square brackets in eq 6 is the contribution from *anisotropic covalency*; it is negative because the metal character in $7b_1(xy)$ is smaller than that in $11a_1(z^2)$. The second term, the contribution from *geometric distortion-induced energy splittings*, is positive for $^4T_{1g}^a$ because the $7b_1(xy)$ MO is higher in energy than the $11a_1(z^2)$ MO, given the more antibonding character of the former.[76] By contrast, in end-on bound Fe(III)-OOH complexes, the main interaction occurs between the peroxide-π_σ^* and Fe-3d$_{z^2}$ orbitals (Scheme 5, right). Thus, both terms in eq 6 change sign and the positive contributions are likely to dominate (Table 6). However, in the limit of vanishing anisotropic covalency, *D* will be negative if the Fe-3d$_{z^2}$ orbital is energetically above Fe-3d$_{xy}$.[75]

As Table 7 shows, the INDO/S-CI calculations reproduce the energies of the first two spin-forbidden quartet states very well, which supports the idea that the negative value for *D* is mainly due to the high covalency of the $7b_1(xy)$ MO.

Finally there is a contribution to *D* from the sextet CT states. In the present case, the only CT state that substantially contributes to *D* is the $^6B_1^b(6b_1'(\pi_\sigma^*) \rightarrow 10a_1(x^2-y^2))$ state. Importantly, this contribution is also negative (Table 6) and depends on the presence of a highly covalent bond, being proportional to the amount of metal character mixed into $6b_1'(\pi_\sigma^*)$. The numerical value is -0.31 cm^{-1} and thus accounts for $\sim$30% of the total *D* value (see supporting information S4 for a listing of individual contributions to *D*).

In summary, substantial anisotropic covalency for the Fe−O σ-bond is required from the analysis of the experimental data and explains the orientation, sign, and magnitude of the observed ZFS tensor.

E. Charge-Transfer Assignments. In this section, CT assignments are given, based on the calculated energies and intensities. We then demonstrate that the polarizations obtained from VTVH-MCD spectroscopy and the excited-states distortions obtained from rR spectroscopy are consistent with these assignments. All transitions are from the $^6A_1^{g.s.}$ ground-state to the various excited states obtained by promoting an electron from a doubly occupied peroxide π^*-based MO into a singly occupied Fe-3d-based MO. The selection rules for these transitions are summarized in Table 8.

The dominant band (band 6) is assigned as a transition to the $^6A_1^b(6b_1'(\pi_\sigma^*) \rightarrow 7b_1(xy))$ excited state. This transition gains most of its intensity via the strong covalencies of the donor (Figure 8E) and acceptor (Figure 8B) MOs,[77] which induce a large dipole moment along the Fe−O_2 direction in the transition

(75) (a) Gebhard, M. S.; Koch, S. A.; Millar, M.; Devlin, F. J.; Stephens, P. J.; Solomon, E. I. *J. Am. Chem. Soc.* **1991,** *113*, 1640. (b) Deaton, J. C.; Gebhard, M. S.; Koch, S. A.; Millar, M.; Solomon, E. I. *J. Am. Chem. Soc.* **1990**, *112*, 2217. (c) Zhang, Y.; Gebhard, M. S.; Solomon, E. I. *J. Am. Chem. Soc.* **1991**, *113*, 5162.

(76) Eq 6 overestimates the negative contributions because it neglects the mixing that occurs between states derived from $^4T_{1g}$ (O_h) and $^4T_{2g}$ (O_h) in low-symmetry environments. However, the principal trends are correctly predicted.

(77) (a) Ros, P.; Shuit, G. C. A. *Theor. Chim. Acta* **1966**, *4*, 1. (b) Solomon, E. I. *Comments Inorg. Chem.* **1984**, *3*, 227.

Table 7. Comparison of Calculated[a] and Measured Excitation Energies and Oscillator Strengths

				ΔE (cm^{-1})		$10^4 f_{osc}$	
state	excitation	pol	%pure	INDO/S	exp	INDO/S	exp (band no.)
$^4B_2^a$	$7b_1(xy)\rightarrow 4a_2(yz)$	−	81	8 020		f	n.d.
$^4B_1^a$	$7b_1(xy)\rightarrow 10a_1(x^2-y^2)$	−	99	8 380	9 540, $^4T_1$	f	n.d. (1)
$^4A_2^a$	$7b_1(xy)\rightarrow 6b_2(xz)$	−	71	8 910		f	n.d.
$^4B_2^b$	$11a_1(z^2)\rightarrow 6b_2(xz)$	−	80	11 950		f	n.d.
$^4A_1^a$	$11a_1(z^2)\rightarrow 10a_1(x^2-y^2)$	−	52	12 620	13 740, $^4T_2$	f	n.d. (2)
$^4A_2^b$	$11a_1(z^2)\rightarrow 4a_2(yz)$	−	68	12 980		f	n.d.
$^6A_2^a$	$3a_2(\pi_\nu^*)\rightarrow 10a_1(x^2-y^2)$	−	82	17 140	n.o.	f	n.o.
$^6A_1^a$	$3a_2(\pi_\nu^*)\rightarrow 4a_2(yz)$	X	82	17 170	18 800	54	40 (3)
$^6B_1^a$	$3a_2(\pi_\nu^*)\rightarrow 6b_2(xz)$	Y	83	18 000		20	
$^6B_1^b$	$6b_1'(\pi_\sigma^*)\rightarrow 10a_1(x^2-y^2)$	Y	96	20 520	21 700	22	84 (4)
$^6B_2^a$	$6b_1'(\pi_\sigma^*)\rightarrow 4a_2(yz)$	Z	96	20 570		14	
$^6A_2^b$	$6b_1'(\pi_\sigma^*)\rightarrow 6b_2(xz)$	−	96	21 550	n.o.	f	n.o.
$^6B_2^b$	$3a_2(\pi_\nu^*)\rightarrow 7b_1(xy)$	Z	97	23 480	n.o.	<1	n.o.
$^6A_2^c$	$3a_2(\pi_\nu^*)\rightarrow 11a_1(z^2)$	−	84	24 390	n.o.	f	n.o
$^6B_1^c$	$6b_1'(\pi_\sigma^*)\rightarrow 11a_1(z^2)$	Y	97	28 930	25,250	77	51 (5)
$^6A_1^b$	$6b_1'(\pi_\sigma^*)\rightarrow 7b_1(xy)$	X	84	34 780	31 050	1300	675−1750 (6)

%pure = weight of the indicated one-electron excitation in the CI expansion for a given state; f = forbidden under the approximations used; n.o.= not observed; n.d.= not determined. [a] Calculations were on **1** by using the ROHF-INDO/S-CIS(D) method.

Table 8. Symmetries for Charge Transfer States from the Peroxide π^* to Fe-3d Transitions in a Side-on Bound FeO_2 Chromophore in C_{2v} Symmetry

	yz	x^2-y^2	*xz*	z^2	*xy*
$\pi_\nu^*\rightarrow$	$^6A_1$ (X)	$^6A_2$ (R_x)	$^6B_1$ (Y,R_z)	$^6A_2$ (R_x)	$^6B_2$ (Z,R_y)
$\pi_\sigma^*\rightarrow$	$^6B_2$ (Z,R_y)	$^6B_1$ (Y,R_z)	$^6A_2$ (R_x)	$^6B_1$ (Y,R_z)	$^6A_1$(X)

[a] Together with electric (*X*,*Y*,*Z*) and magnetic dipole (R_x,R_y,R_z) selection rules for transitions from the $^6A_1$ ground-state for the coordinate system described in the text.

density[78] and therefore lead to *x*-polarized CT intensity. The calculated energy of this transition is ~3000 cm^{-1} higher than observed experimentally in the frozen state and ~1000 cm^{-1} higher than observed in the room-temperature spectrum (see Section 2 and Table 7). The calculated oscillator strength (Table 7) is intermediate between the upper and lower limits of the experimental estimate (Tables 1, 7), which again indicates that the calculated covalency is reasonable.

Band 5 is assigned to the $^6B_1^c(6b_1'(\pi_\sigma^*)\rightarrow 11a_1(z^2))$ state. The calculated energy of this band is again ~3000 cm^{-1} higher than observed in the low-temperature ABS spectra. The calculated oscillator strength of this band is in good agreement with the experimental value (Table 7). It is explained by the mixing of Fe-d_{z^2} orbital with the peroxide π_σ^b-FMO, which gives the transition a small amount of intraligand $\pi^*\rightarrow\pi$ character and therefore a nonvanishing transition dipole moment in the *y*-direction. Thus, the intensity of band 5 is additional experimental evidence for a bonding description in which the interaction of the iron 3d orbitals with the bonding peroxide orbitals is much stronger than with the high-lying peroxide σ^*-FMO.

Bands 3 and 4 are assigned to CT transitions into the t_{2g}-derived orbitals $10a_1(x^2-y^2)$, $6b_2(xz)$, and $4a_2(yz)$. Band 3 is assigned to the $^6A_1^a(3a_2(\pi_\nu^*)\rightarrow 4a_2(yz))$ state. This is reasonable, based on the expectations that the $3a_2(\pi_\nu^*)$ MO is less stabilized than the $6b_1'(\pi_\sigma^*)$ MO and that the first CT transition in the spectrum should originate from the $3a_2$ MO (Figure 7). This transition is polarized along the *x*-direction and again gains most of its intensity by the covalencies of the donor and acceptor MOs. However, this mixing is small and therefore the CT intensity is expected to be weak, as was observed experimentally (Table 1) and calculated (Table 7). Band 4 is calculated as a composite band consisting of contributions from $^6B_1^a(3a_2(\pi_\nu^*)\rightarrow 6b_2(xz))$ and $^6B_1^b$ $(6b_1'(\pi_\sigma^*)\rightarrow 10a_1(x^2-y^2))$, which are both *y*-polarized, as well as from $^6B_2^a(6b_1'(\pi_\sigma^*)\rightarrow 4a_2(yz))$, which is *z*-polarized and calculated to be weak (Table 8). The calculated energies of these states are fairly close to but slightly lower than the experimental ones. Together with the slightly overstimated energies for bands 5 and 6, this indicates that the main shortcoming of the calculation is its overestimation of the t_{2g}/e_g orbital splitting (i.e., 10 Dq) by ~3000 cm^{-1}; however, the qualitative agreement between the experimental and calculated spectra is excellent.

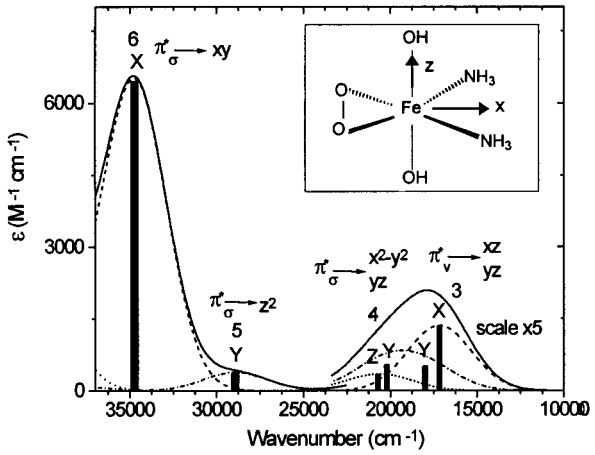

Figure 10. Analysis of the calculated ABS spectrum from an ROHF−INDO/S-CIS(D) calculation on **1** as described in the text. (−) total absorption intensity, (- - -) Fe−O (*x*) polarized intensity, (-.-.-.-) O−O (y) polarized intensity, and (.....), out-of-plane (*z*) polarized intensity.

F. Origin of MCD Spectral Features and Polarizations. There is no three-dimensional structural information for the Fe(III)−EDTA−peroxide complex available because crystals of this molecule have not yet been obtained. For the same reason, polarized single-crystal ABS and MCD measurements are not possible; rather, all spectroscopy has been carried out on samples with randomly oriented molecules in the frozen state. Nonetheless, a detailed analysis of the VTVH-MCD data still allows the determination of the transition polarizations on

(78) McWeeny, R. *Methods of Molecular Quantum Mechanics*; Academic Press: London, 1992; chapter 5.

randomly oriented samples. This is an invaluable aid in assigning experimental spectra and obtaining insight into the nature of the excited states under consideration.

To observe nonzero MCD *C*-term intensity in a transition, it must have transition dipole moment components in two orthogonal directions.[79] Thus, in orthorhombic and lower-symmetry groups, including C_{2v}, where all transitions are unidirectional, *C*-term intensity cannot arise unless there is a mechanism that mixes an orthogonal transition moment into a given allowed transition. The dominant mechanism in providing the required "off axis" intensity is SOC.[46,79] In the case of high spin Fe(III) complexes, there is no spin-allowed ligand field transition, and the main SOC that occurs for the ground-state arises from the lowest excited quartet states, which also make the dominant contribution to the ZFS.[75] Since the selection rule for electric dipole transitions is $\Delta S = 0$,[78,79] this mixing does not give rise to any extra intensity in the spin-allowed CT transitions. On the other hand, the SOC between different allowed CT excited states does mix transitions of orthogonal polarization and provides a basis for the interpretation of the experimentally observed *C*-term intensity. The reason for choosing the coordinate system in Figure 10 for the description of the electronic structure is now apparent: It is the principal coordinate system of the **D**-tensor and is therefore the one that was implicitly referred to by choosing the spin-Hamiltonian eq 1 in the analysis of the experimental VTVH-MCD data in Section 3. We can therefore directly compare the polarization information obtained in Section 3 with the predicted polarizations summarized in Table 8.[80]

In Figure 10, band 3 was assigned to the $^6A_1^a(3a_2(\pi_\sigma^*) \rightarrow 4a_2(yz))$ excited state, which is *x*-polarized. This state spin−orbit couples with states of $^6B_1$ symmetry, which are *y*-polarized, via the *z*-component of the SOC operator. There are two such states close to band 3 (Table 7). However, only $^6B_1^a(3a_2(\pi_\nu^*) \rightarrow 6b_2(xz))$ will be effective because the alternative $^6B_1^b(6b_1'(\pi_\sigma^*) \rightarrow 10a_1(x^2-y^2))$ differs by a 2-electron jump from $^6A_1^a(3a_2(\pi_\nu^*) \rightarrow 4a_2(yz))$. Thus, the *x*-polarized $^6A_1^a(3a_2(\pi_\nu^*) \rightarrow 4a_2(yz))$ state gains some allowedness in the *y*-direction by SOC with $^6B_1^a(3a_2(\pi_\nu^*) \rightarrow 6b_2(xz))$ and the transition will be strongly x,y-polarized. From Section 3, this is precisely what is observed with band 3, which is >99% *x*,*y*-polarized and thus supports this assignment. As discussed in Section 3.C, the experimental data do not allow the separate evaluation of the %*x* and %*y* polarizations. Although dominant *x*-polarization is expected for band 3 from the nature of the "pseudo-A" mechanism and the results for band 4 (see below), this outcome cannot be experimentally defined. Note that from our MO calculations the sign of band 3 is predicted to be positive and that of band 4 to be negative, as was observed experimentally (supporting information S7).

Experimentally, band 4 is ∼90% *y*-polarized, ∼8% *x*-polarized, and ∼2% *z*-polarized. Thus the main source of intensity must be the states of $^6B_1$ symmetry (Table 8). From the sum rule,[79,81] it is $^6B_1^a(3a_2(\pi_\nu^*) \rightarrow 6b_2(xz))$ that must make the largest contribution, via the SOC with $^6A_1^a(3a_2(\pi_\nu^*) \rightarrow 4a_2(yz))$ as described above. The nature of this pseudo-A intensity mechanism necessitates that the *C*-term sign for $^6B_1^a(3a_2(\pi_\nu^*) \rightarrow 6b_2(xz))$ be opposite that of $^6A_1^a(3a_2(\pi_\nu^*) \rightarrow 4a_2(yz))$, which explains the derivative-shaped MCD for bands 3 and 4 in Figures 2 and 3.[79,81] The *z*-polarized intensity must originate from the contributions of the $^6B_2^a(6b_1'(\pi_\sigma^*) \rightarrow 4a_2(yz))$ state because this is the only CT state with *z*-polarization in this spectral region. This state will not spin−orbit couple with $^6B_1^a(3a_2(\pi_\nu^*) \rightarrow 6b_2(xz))$ because these differ by a 2-electron jump, but a nonvanishing SOC occurs with $^6B_1^b(6b_1'(\pi_\sigma^*) \rightarrow 10a_1(x^2-y^2))$ via the *x*-component of the SOC operator. Thus, for the *z*-polarized intensity to be observed, both $^6B_1^b(6b_1'(\pi_\sigma^*) \rightarrow 10a_1(x^2-y^2))$ and $^6B_2^a(6b_1'(\pi_\sigma^*) \rightarrow 4a_2(yz))$ must have electric dipole intensity and therefore must also contribute to the absorption intensity in the region of band 4.

Finally band 6, which is assigned to the $^6A_1^b(6b_1'(\pi_\sigma^*) \rightarrow 7b_1(xy))$ state and is expected to be *x*-polarized (Table 8), is experimentally seen to have ∼98% *x*,*y* and ≈2% *z*-polarization, which again supports this assignment. Since the C-term intensity for band 6 is at least 1 order of magnitude stronger than for bands 1 through 5, the origin of its intensity cannot be spin−orbit mixing with any of the lower-energy states. Therefore, the intensity mechanism requires SOC to higher-energy states. The density of states increases rapidly above band 6 and experimental information for these is lacking. However, a reasonable candidate to contribute the required *y*-polarized intensity is the transition to $^6B_1(8a_1(\pi_\sigma^b) \rightarrow 7b_1(\pi_\sigma^*))$, which is of the correct symmetry and carries the covalency necessary for SOC mixing with the $^6A_1^b(6b_1'(\pi_\sigma^*) \rightarrow 7b_1(xy))$ state. The *z*-polarized intensity might originate from a coupling to LMCT transitions from the axial ligands, which are close in energy and partially overlap with band 6.

To summarize, the polarizations extracted from VTVH-MCD data on samples containing randomly oriented molecules strongly support the assignment of bands developed in the previous section and presented in Figure 10. Band 6 is the $^6A_1^b(6b_1'(\pi_\sigma^*) \rightarrow 7b_1(xy))$ *x*-polarized state, band 3 is attributable to the $^6A_1^a(3a_2(\pi_\nu^*) \rightarrow 4a_2(yz))$ *x*-polarized state, and band 4 is a composite band that involves contributions from the $^6B_1^a(3a_2(\pi_\nu^*) \rightarrow 6b_2(xz))$ *y*-polarized, $^6B_1^b(6b_1'(\pi_\sigma^*) \rightarrow 10a_1(x^2-y^2))$ *y*-polarized, and the $^6B_2^a(6b_1'(\pi_\sigma^*) \rightarrow 4a_2(yz))$ *z*-polarized excited states.

G. Origin of Excited-State Distortions. Figure 11 presents calculated potential energy surfaces along the O−O stretching coordinate for all 10 peroxide-π*-to-Fe(III) LMCT transitions. As already determined from the rR results (Table 3, Section 4), bands 3 and 4 represent "normal" CT transitions with ferrous-superoxide-like excited states. The calculations show that except for the $^6A_1^b(6b_1'(\pi_\sigma^*) \rightarrow 7b_1(xy))$ state to be discussed below, all LMCT states give rise to similar excited-state distortions with O−O bond length changes in the range −0.125 to −0.145 Å, in excellent agreement with the experimentally derived values (Table 3). Fitting Morse potential curves to the data (supporting information S5) shows that the O−O force constants in the excited states increase by ∼2-fold, which corresponds to an increase of ∼40% in the excited-state O−O vibrational frequency, again emphasizing the superoxide-like character of the O_2 ligand in the CT states.

The $^6A_1^b(6b_1'(\pi_\sigma^*) \rightarrow 7b_1(xy))$ state behaves rather differently (top trace in Figure 11) and has a very small calculated excited-state O−O distortion of −0.045 Å, again in good agreement with the experimental results for band 6. The origin of this effect is that the donor and acceptor MOs both have very similar

(79) (a) Piepho, S. B.; Schatz, P. N. *Group Theory in Spectroscopy with Applications to Magnetic Circular Dichroism*; John Wiley: New York, 1983. (b) Stephens, P. J. *Annu. Rev. Phys. Chem.* **1974**, *25*, 201. (c) Stephens, P. J. *Adv. Phys. Chem.* **1976**, *35*, 197.

(80) Under the aproximations considered here, the percentage x-polarized intensity is given by $\%x = 100 \times M_{xy}^2M_{xz}^2(M_{xy}^2M_{xz}^2 + M_{xy}^2M_{yz}^2 + M_{xz}^2M_{yz}^2)^{-1}$ and cyclic permutations of indices for the %*y*- and %*z*-polarizations, respectively.

(81) Gerstman, B. S.; Brill, A. S. *J. Chem. Phys.* **1985**, *82*, 1212.

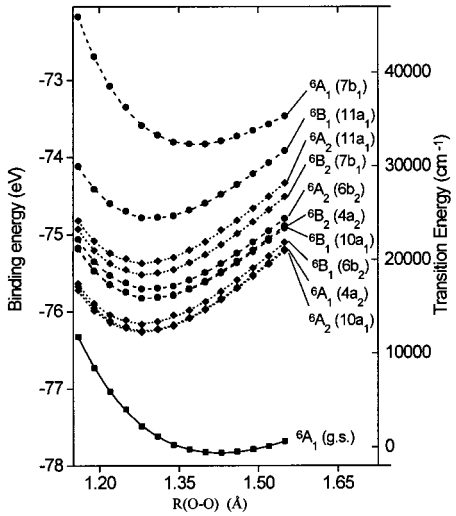

Figure 11. Potential energy surfaces for the peroxide-to-iron LMCT transitions evaluated along the O−O stretching coordinate. The total ground-state binding energy (left axis) was obtained from gradient-corrected DFT calculations. The ROHF−INDO/S-CIS(D) transition energy was added to this energy at each point to obtained the excited-state surfaces. (- - -) Morse potential curve fits to the π^*_σ to iron LMCT transitions (....) Morse potential curve fits to the π^*_ν to iron LMCT transitions. Acceptor MOs are indicated in parentheses.

antibonding character with respect to the O−O bond ($7b_1(xy)$ and $6b_1'(\pi^*_\sigma)$ top right in Figure 9) and therefore the displacement of the ground- and excited-state potentials along the O−O bond is very small. Thus, the weak enhancement of the ν_{OO} feature observed experimentally for band 6 is a direct consequence of the high covalency of the iron−peroxide σ-bond. Alternatively, this transition formally eliminates the main contribution to the stability of the iron−peroxide bond and therefore the Fe−O distortion is very large.

Thus, it is the specific combination of donor and acceptor MOs that determine the magnitude of an excited-state distortion rather than either the donor or the acceptor MO alone. The observed excited-state distortions support our assignment of excited states developed above and summarized in Table 7.

Discussion

This study develops a detailed description of the electronic structure of a mononuclear high-spin η^2-peroxide−ferric complex by a combination of spectroscopic and theoretical techniques. The main conclusions are as follows: (a) The ferric−peroxide interaction is dominated by a strong, covalent σ-donor bond formed between the π^*_σ and Fe-d_{xy} orbitals; (b) interactions of π- and δ-symmetry are weak; (c) there is no back-bonding with the peroxide σ*-orbital, and the O−O bond is not activated beyond the peroxide level; (d) instead, there are additional moderate donor interactions between filled peroxide π^b-orbitals and the iron. The spectroscopic data support this description such that the electronic structure can now be used to obtain insight into the reactivity of this and related non-heme peroxo−iron complexes.

Characteristic Spectral Features. The zero-field splitting measured by EPR or Mössbauer spectroscopy is characterized by a negative D value that is directly related to the high anisotropic covalency of the Fe−O_2 σ-bond. The covalency attenuates the magnetic moment perpendicular to the x,y-plane and therefore lowers D_{zz}; thus, $D = D_{zz} - 1/2(D_{xx} + D_{yy}) < 0$. The CT spectrum is dominated by a strong band around 31 000 cm^{-1} that originates from a $\pi^*_\sigma \rightarrow$Fe-d_σ transition. The weak CT transitions found in the visible part of the spectrum give the complex its characteristic purple color and reflect the weak π-interactions that are characteristic of the η^2-FeO_2 arrangement. This bonding pattern is also reflected in the rR profiles, which show strong enhancement of the O−O stretching vibration in the visible region and weak enhancement under the intense UV band. In contrast, the Fe−O stretching vibration is greatly enhanced under the UV band but only moderately in the visible region.

Table 9. Comparison of Optical and Vibrational Parameters for Several Copper and Iron−Peroxo Complexes

type of bonding	$\sum_i f_i$	$\sum_i f_i/\nu_i$	ν_{OO} (cm^{-1})	f_{OO} (mdyn/Å)
Cu end-on OOH monomer	0.105	537	803	2.9
Cu trans-μ-1,2 dimer	0.252	1350	832	3.1
Cu μ:η^2:η^2 dimer	0.479	1730	763	2.4
Fe cis μ-1,2 dimer	0.183	944	876	3.1
	(0.135)	(760)		
Fe η^2 monomer	0.196	660	816	3.0−3.1
	(0.089)	(350)		

f_i is the oscillator strength of a transition which peaks at frequency ν_i (in cm^{-1}) and the sum is over all peroxide-to-metal CT transitions. Data for copper complexes and the Fe cis-μ-1,2 dimer are from Brunold et al.[72] Values in parentheses represent lower limits.

Comparison with cis-μ-1,2-Peroxo-Bridged Diferric Complexes. A detailed study of the electronic structure of a cis-μ-1,2-peroxo-bridged diferric complex (i.e., *cis*-μ-1,2-Fe_2O_2 dimer) has recently been reported[72] that serves as an interesting comparison to the present work. In peroxide complexes, the total peroxide donor strength can be estimated by a weighted sum over the oscillator strengths of the peroxide-to-iron LMCT transitions.[56]

$$\text{Donor strength} \propto \sum_i f_i/\nu_i \qquad (7)$$

where f_i is the oscillator strength of the ith transition centered at frequency ν_i. In Table 9 are compared the optical and vibrational parameters observed for several Cu(II) and Fe(III) peroxo complexes. Comparison of the η^2-FeO_2 monomer and the *cis*-μ-1,2-Fe_2O_2 dimer[72] reveals that the sum of the oscillator strengths is comparable for the two systems but, on weighting with the inverse transition energies, the total donor strength is higher for the latter (Table 9). This is explained by the very different bonding schemes for the two molecules. Whereas the *cis*-μ-1,2-Fe_2O_2 dimer has a strong π- and only moderate σ-interactions between the peroxide-π* and Fe-3d orbitals,[72] the reverse is true for the η^2-FeO_2 monomer. Thus the *cis*-μ-1,2-Fe_2O_2 dimer has most of its CT intensity in the peroxide-to-iron $\pi^*_\nu \rightarrow$Fe-d_π transition at low transition energies (~14 600 cm^{-1})[72], whereas in the η^2-FeO_2 monomer the high-intensity transition is of the peroxide-to-iron $\pi^*_\sigma \rightarrow$Fe-d_σ type and is centered at higher energies (~31 000 cm^{-1}, Table 7).

This very different balance of π- and σ-donor interactions is also demonstrated by the rR profile behavior. For the *cis*-μ-1,2-Fe_2O_2 dimer, strong resonance enhancement of the Fe−O stretching vibration is observed for the low-energy/high-intensity transitions and weak enhancement for the high-energy/low-intensity transitions.[72] Again, this reflects a strong π-/weak σ-bond between peroxide and iron,[72] whereas the side-on geometry leads to a strong σ-/weak π-bonding pattern. Consequently, enhancement of the Fe−O stretching vibration is strong under the high-energy/high-intensity band and weak for excitation into the low-energy/low-intensity bands.

Despite their different bonding schemes, the O−O force constants for the η^2-FeO_2 monomer and the *cis*-μ-1,2-Fe_2O_2

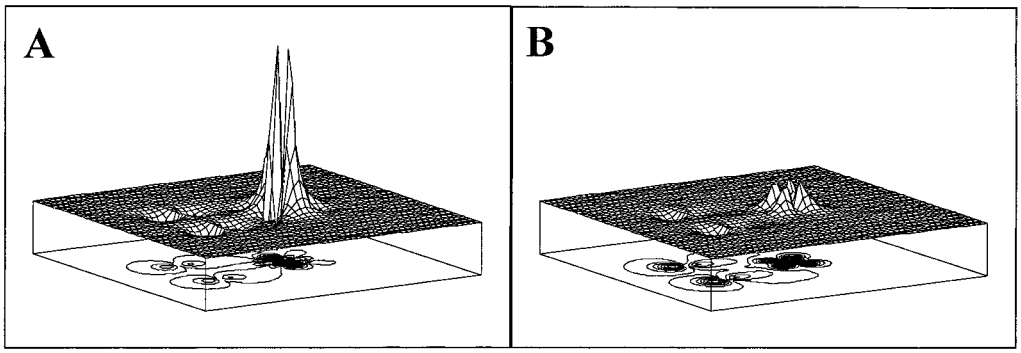

Figure 12. Plots showing the difference in total electron density between the excited states and the ground-state evaluated from the ROHF−INDO/S-CIS(D) wave functions. Both plots are on the same scale. (A) $^6B_1^b(6b_1'(\pi_\sigma^*)\rightarrow 10a_1(x^2-y^2))$, (B) $^6A_1^b(6b_1'(\pi_\sigma^*)\rightarrow 7b_1(xy))$. The two negative dots on the left side are at the positions of the two oxygen atoms, indicating removal of electron density in the excited state. The positive region is at the position of the Fe-atom, indicating an increase in electron density in the excited state.

dimer are almost identical (Table 9). This is a surprising result because the observed vibrational energy for the ν_{OO} mode is significantly higher for the *cis*-μ-1,2-Fe_2O_2 dimer ($\sim$60 cm^{-1}, Table 9). However, as pointed out by Brunold et al.,[72] this frequency is severely influenced by mechanical coupling between the Fe−O and O−O stretching modes in the latter case. Therefore, the energy of the ν_{OO} mode does *not* directly reflect the intrinsic stiffness of the O−O bond in the case of *cis*-μ-1,2-Fe_2O_2 dimer but it does for the η^2-FeO_2 monomer. From eq 7 and Table 9, the total donor strength appears to be somewhat higher for the *cis*-μ-1,2-Fe_2O_2 dimer, which implies that the O−O stretching force constant should be be larger in this molecule, given that the electrons are donated mainly from peroxide-π* orbitals. That this is not the case might arise from the donor function of the peroxide-π_σ^b orbital in the η^2-FeO_2 monomer, which would tend to compensate the π_σ^* donation somewhat.

Comparison with μ:η^2:η^2 Peroxo-Bridged Dicopper Complexes. In terms of binding geometry, the η^2-FeO_2 complex is closest to the μ:η^2:η^2-Cu_2O_2 complexes of the oxyhemocyanin type.[57] Yet the donor strength of the iron complex is considerably lower (Table 9). This is partly because of the increased number of donor interactions in μ:η^2:η^2-Cu_2O_2 complexes (four, vs two in η^2-FeO_2) but also because of the high effective nuclear charge of copper and the generally lower coordination number of copper complexes, both of which facilitate donor interactions with the peroxo ligand.[73] The latter two factors are expected to be quite general and are also consistent with the fact that the donor strengths of the *trans*-μ-1,2-Cu_2O_2 complex is larger than that of the *cis*-μ-1,2-Fe_2O_2 system.[72] Despite these general factors, the total donor strength in the η^2-FeO_2 geometry is at least as large as or larger than that in the end-on Cu−OOH arrangement (Table 9). Clearly, OOH^- is a much poorer donor ligand than O_2^{2-}—which is also consistent with the results from our calculations on monomeric iron−hydroperoxide complexes.

Both the rR enhancement pattern of the ν_{OO} and ν_{FeO} modes and the distribution of CT intensity in the η^2-FeO_2 monomer most closely resemble the spectral features of the μ:η^2:η^2-Cu_2O_2 core of oxyhemocyanin. In both cases there is a relatively low CT intensity in the visible region that is mostly attributed to peroxide-π_ν^*-to-metal CT transitions, which mainly enhance the O−O stretching vibration because the relevant excited states have much superoxide character. Alternatively, both η^2-complexes show a high CT intensity in the near-UV region, which is associated with strong enhancement of the metal−ligand stretching vibration and only moderate enhancement of the O−O stretching vibration. An explanation of this effect is given in Figure 12. Figure 12 shows the difference in the total electron density between a CT excited state and the ground-state in the FeO_2 plane of the η^2-FeO_2 monomer.[82] In particular, the $\pi_\sigma^*\rightarrow$Fe-d_σ CT transition (Figure 12B) leads to a much smaller change in the total electron density than does the $\pi_\sigma^*\rightarrow$Fe-d_π excited state (Figure 12A). This is attributable to the high covalency of the side-on FeO_2 bond. The total electron density does not change much in the former case because the donor (π_σ^*+Fe-d_{xy}) and acceptor MOs (π_σ^*-Fe-d_{xy}) are both shared relatively evenly by the metal and the peroxide. However, an electron in an FeO_2-bonding MO is excited to a strongly antibonding FeO_2 MO, which produces a large distortion of the FeO_2 bond, as has been observed experimentally. By contrast, in the $\pi_\sigma^*\rightarrow$Fe-d_π excited state, an electron is promoted from a bonding MO (π_σ^* + Fe-d_{xy}) into an essentially nonbonding MO (Fe-$d_{x^2-y^2}$); therefore, there is a large change in the charge density and in the O−O bonding character, leading to a stronger enhancement of the O−O stretching vibration and moderate enhancement of the metal−ligand stretch. Similarly, the amount of CT will be larger for transitions that originate from the π_ν^* orbital than from the π_σ^* orbital.

Despite the similar nature of the dominant CT excited state, there is an important difference in the electronic structures of the η^2-FeO_2 monomer and μ:η^2:η^2-Cu_2O_2 dimer, which is reflected in their O−O stretching force constants (Table 9). The exceptionally low force constant (i.e., weak O−O bond) in the μ:η^2:η^2-Cu_2O_2 dimer arises from an electron back-donation from the copper to the strongly antibonding peroxide-σ* orbital.[56,57] As developed in this paper, such an interaction is absent in the η^2-FeO_2 monomer because of the high effective charge on the ferric ion and the substantial exchange stabilization of the high-spin d^5 configuration.[73,74] Consequently, the O−O bond is significantly stronger in the η^2-FeO_2 monomer.

Formation and Structure. Fe(III)−EDTA is known to exist in two isomeric, 7-c forms in the solid state[83] and is believed to retain its structure in solution.[18] The coordinated water in

(82) To facilitate the comparison, two transitions are chosen that are both polarized along the Fe−O_2 bond direction and have the donor and acceptor MOs concentrated in the FeO_2 plane. Thus the main changes in the electron density occur in this plane for both transitions.

(83) (a) Hamor, M. J.; Hoard, J. L. *Inorg. Chem.* **1964**, *3*, 34. (b) Kennard, C. H. L. *Inorg. Chim. Acta* **1967**, *1*, 347. (c) Oakes, J.; Smith, E. G. *J. Chem. Soc., Faraday Trans. 1* **1983**, *79*, 543. (d) Solans, X.; Font-Altaba, M.; Garcia-Oricain, J. *Acta Crystallogr.* **1985**, *C41*, 525. (e) Mizuta, T.; Yamamoto, T.; Miyoshi, K.; Kushi, Y. *Inorg. Chim. Acta* **1990**, *175*, 121.

Scheme 6

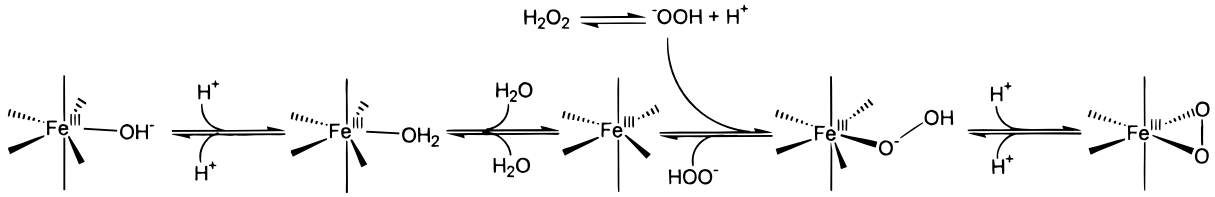

the seventh coordination position has a pK_a of 7.6.[84] A second ionization, occurring around pH 10.2, was attributed to binding of an additional OH^-,[84b] but a subsequent analysis showed that this result is probably wrong.[15b] The first pK_a of H_2O_2 is 11.6,[85] therefore, under our experimental conditions, a substantial amount of O_2H^- is present. Since the formation of the complex is known to liberate 1 equivalent of acid,[13b,16a] the reaction is most-conveniently formulated:[13,15,16]

$$H_2O_2 \rightarrow HOO^- + H^+ \quad (8a)$$

$$[Fe-EDTA-OH]^{2-} + O_2H^- \rightarrow [Fe\text{-}EDTA\text{-}O_2^{2-}]^{3-} + OH^- + H^+ \quad (8b)$$

The rate of formation is subject to general acid and base catalysis but is independent of pH in a region where the O_2H^- concentration increases by an order of magnitude,[15] which implies that O_2H^- is not involved in the rate-determining step. A scheme that accounts for these data as well as for the inverse dependence of the equilibrium constant on pH[16] is similar to that proposed by Bull et al.[15b] (Scheme 6).

In this scheme the hydroxy-complex is not reactive, but protonation is known to lead to a rapidly exchanging water molecule (residence time $\approx 1.3 \times 10^{-6}$ s),[86] and the reaction could be driven to the right by binding and deprotonation of the hydroperoxo anion. According to NMR water-relaxation studies,[17c] the OH^- might be able to remain in the coordination sphere of the peroxo complex, but reconciling this suggestion with the scheme of Bull et al.[15b] appears difficult. Based on the binding constant of 10^3-10^4,[13,16] reactions 8a and b have an overall Gibbs free energy change ($\Delta G°$) of -4 to -5.5 kcal/mol. This implies that the binding of the peroxide greatly lowers the second pK_a of H_2O_2. That this is not unreasonable is shown by a μ-1,1-hydroperoxy dicobalt(III) complex, for which the pK_a of the bridging hydroperoxide is estimated to be $\sim$11.[87]

From our results, the driving force for deprotonation of the hydroperoxide can be explained by the formation of a strong, covalent Fe$-$O$_2$ σ-bond, given that O_2^{2-} is a much better donor than ^-O_2H (vide supra). Furthermore, the result that the complex is best described as 6-c implies that two arms of the EDTA ligand may dissociate on formation of the η^2-FeO_2 bond.

Correlation with Reactivity. The fact that the FeO_2 bond is very covalent implies a significant charge donation to the iron atom and therefore a substantial drop of the potential of the Fe(II)/Fe(III) couple. Thus, the complex will be difficult to reduce and the O$-$O bond is not activated for reductive cleavage. Furthermore, the result that the O$-$O bond is *not* weakened by back-bonding interactions implies that the O$-$O bond is not activated for direct cleavage. Although the O_2^{2-}-ligand loses some of its electron density on bond formation, the charge donation is less than in the $[Cu_2(XYL\text{-}O)O_2]$ complex, which exhibits nucleophilic reactivity.[88] Thus, the η^2-FeO_2 monomer is more nucleophilic than the latter complex, and protonation of the O_2^{2-} ligand, as observed in $[Cu_2(XYL\text{-}O)O_2]$[88] and related Co-peroxide complexes,[87] appears to be the likely first step in the activation of the complex, as opposed to the direct attack of organic substrates. The protonation could occur via the favorable interaction of a proton with the π_v^*-orbital, which is not stabilized by bonding interactions with the iron.

Scheme 7

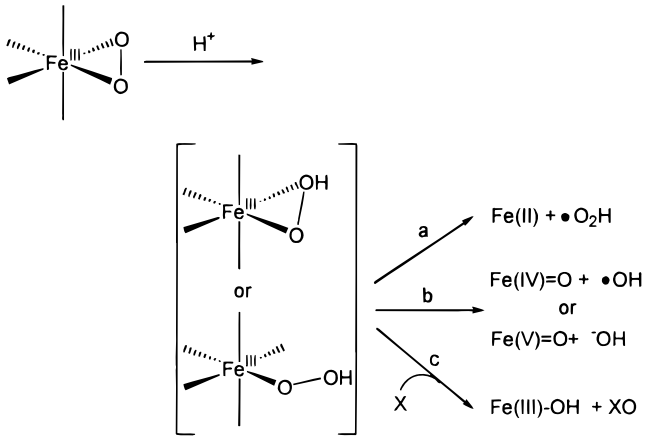

These suggestions are in agreement with the known chemistry of the Fe(III)$-$EDTA$-$peroxide system.[14−17] Under conditions of reasonable stability, the complex is inert against strong 1- and 2-electron reductants such as $Na_2S_2O_4$ and $NaBH_4$,[15] which shows that the potential of the Fe(II)/Fe(III) couple must be substantially lower than that of the Fe(III)$-$EDTA precursor ($\sim +0.120$ mV below and $\sim +0.068$ V above pH 8[84b]). In alkaline solution (pH $>$ 10.5), the complex is found to be unreactive toward organic substrates but can slowly decompose H_2O_2 to O_2 and H_2O.[16] However, vigorous reactivity observed at lower pH ($<$10.5) leads to the decomposition of excess EDTA to CO_2 and NH_3 as well as the attack of other organic substrates.[16] These findings, together with kinetic results,[17] are consistent with the idea that the first step is the protonation of the bound peroxide to obtain a high-spin Fe(III)$-$hydroperoxide intermediate. This intermediate could undergo several of the types of reactivity shown in Scheme 7a$-$c.

Traditionally, the decomposition of hydrogen peroxide by ferric complexes has been assumed to proceed by redox and radical chain reactions.[16,89] In the present case, such a chain would be initiated by the decay of the peroxo-complex to

(84) (a) Gustafson, R. L.; Martell, A. E. *J. Phys. Chem.* **1963**, *67*, 576. (b) Schwarzenbach, G.; Heller, J. *Helv. Chim. Acta* **1951**, *34:65*, 576.

(85) Holm, R. H.; Kennepohl, P.; Solomon, E. I. *Chem. Rev.* **1996**, *96*, 2239.

(86) Bloch, J.; Navon, G. *J. Inorg. Nucl. Chem.* **1980**, *42*, 693.

(87) (a) Mori, M.; Weil, J. A. *J. Am. Chem. Soc.* **1967**, *89*, 3732. (b) Thewalt, U.; Marsh, R. *J. Am. Chem. Soc.* **1967**, *89*, 6364. (c) Davies, R.; Sykes, A. G. *J. Chem. Soc. A* **1968**, 2840. (d) Davies, R.; Stevenson, M. B.; Sykes, A. G. *J. Chem. Soc. A* **1970**, *1261*.

(88) (a) Tyeklar, Z.; Karlin, K. D. In *Dioxygen Activation and Homogeneous Catalytic Oxidation*, Simandi, L. I., Ed.; Elsevier Science Publishers: Amsterdam, 1991, pp 237−248. (b) Paul, P. P.; Tyeklar, Z.; Jacobson, R. R.; Karlin, K. D. *J. Am. Chem. Soc.* **1991**, *113*, 5322.

(89) Barb, W. G.; Baxendale, J. H.; George, P.; Hargrave, K. R. *Trans. Faraday Soc.* **1951**, *47*, 591.

Fe(II)−EDTA and superoxide (Scheme 7a). The chain could be propagated by standard Fenton chemistry,[16,89] and the primary agent that attacks organic substrates would be the OH$^\bullet$ radical.[90] EPR signals that are consistent with superoxide ions have been observed in the Fe(III)−EDTA−peroxide system[18c] and also in our spectra (data not shown). The product distribution and reactivity patterns obtained by Walling and co-workers are largely consistent with such a scheme,[16] and EPR experiments have identified spin-trap adducts that are consistent with OH$^\bullet$ radicals.[91] However, in the latter study, additional reactivity was demonstrated that could not be explained this way.

As an alternative to radical chain reactions in ferric−peroxide systems, metal-based active oxygen species have been postulated (Scheme 7b).[1e,17e,60,90b,c,91−96] In relation to the well-studied heme systems,[5,6] one could reasonably assume that such a species would be highly reactive toward organic substrates. However, a key question related to the existence of a high-valent iron-oxo intermediate in a mononuclear non-heme environment is the source of its stability. In iron−porphyrins, an extra oxidation equivalent is delocalized into the porphyrin ring to produce a species that is best described as $(P^{-\bullet})(FeO)^{2+}$ rather than $(P^{2-})(FeO)^{3+}$.[5,6] In binuclear diferric enzymes, the second metal can play the role of the porphyrin, and breakdown of an Fe(III)$_2$-μ-peroxo to an Fe(IV)$_2$-bis-μ-oxo species (intermediate Q[97]) should be feasible because of the formation of favorable oxo-bridges.[98] By contrast, mononuclear ferric complexes and active sites lack this possibility and would thus lead either to a species that is described as $(FeO)^{3+}$ or to an $(FeO)^{2+}$-ligand radical. Given that the redox potential of an $(FeO)^{2+}$ species has been estimated to $\geq$1 V[99] ($\sim$0.9 V in compound **II**[5,6]), that of an $(FeO)^{3+}$ species must be considerably higher; such a species may be expected to show rather indiscriminate reactivity, which could be fatal in a biological environment.

An alternative to high-valent intermediates and radical schemes is the possibility that the ferric−hydroperoxide could itself be a highly reactive species (Scheme 7c),[1e,60,92,93a] possibly even in the case of some iron porphyrins.[1e,100,101] This proposal is attractive because such a species potentially leads to more-selective reaction products than do Schemes 7a,b. Although this possibility requires much more experimental and theoretical work, some results in the literature are compatible with the presence of active oxygen species that are more selective than OH$^\bullet$ radicals. Activated bleomycin, the final intermediate kinetically competent to selectively cleave DNA,[4] has been shown to be a low-spin Fe(III)−hydroperoxide complex.[102] Other examples are provided by (a) the epoxidation of a number of olefins by iron−cyclam complexes,[93a] (b) the observation that the product distribution in alkane functionalization studies can be controlled by the peroxide concentration,[92] and (c) the site-selective cleavage of proteins with a covalently attached Fe−EDTA derivative in the presence of H_2O_2.[16e,103] Moreover, recent post-Hartree−Fock calculations support the possibility that oxygen atom transfer reactions by ferric−hydroperoxide species could be kinetically feasible. The barrier of O-transfer from $[Fe(NH_2)_2OOH]$ to NH_3 was calculated to be only 10.2 kcal/mol.[104]

An important example of the activation of a peroxide ligand for heterolytic O−O bond cleavage through protonation is provided by the μ-amido-μ-1,2-peroxo dicobalt(III) dimer.[87] In this complex, the unprotonated peroxo-ligand is unreactive; however, protonation leads to the μ-amido-μ-1,1-hydroperoxo dicobalt(III) complex, which reacts with Cl^- and Br^- ions to produce the μ-amido-μ-1,1-hydroxy dicobalt(III) complex, OCl^-, and OBr^-.[87] In these reaction systems the active species is the hydroperoxy−metal complex, and there is no need to invoke high-valent intermediates or radical chains.

Finally, we note that Valentine and co-workers have studied the reactivity of ferric peroxo−heme complexes,[101] which are also believed to have a side-on structure.[12] They concluded that the peroxo ligand in these complexes displays nucleophilic rather than electrophilic reactivity. The nucleophilicity has been proposed to be modulated by axial ligands, which may lead to an open form of the peroxide complex.[101] However, significant differences are likely to exist between the reactivities of heme and non-heme systems.

In summary, the side-on ferric peroxide bond appears to be most-efficiently activated for reactivity by protonation. The resulting high-spin ferric hydroperoxide intermediate can undergo a variety of further reactions, and it is possible or even likely that more than one mode of reaction is typically observed in experiments. Enzyme active sites with their ability to control acid/base chemistry and create hydrophobic pockets are ideally suited to carry out this chemistry in a selective manner. Electrophilic reactions such as oxygen atom transfer of ferric−hydroperoxide species are very attractive alternatives to free-radical or high-valent iron-based reaction schemes. Further experimental and theoretical investigations are now underway to evaluate these possibilities.

(90) (a) Pogodolski, W. K.; McNeese, T. J.; Tullius, T. D. *J. Am. Chem. Soc.* **1995**, *117*, 6428. (b) Luzzatto, E.; Cohen, H.; Stockheim, C.; Wieghardt, K.; Meyerstein, D. *Free Rad. Res.* **1995**, *23*, 453. (c) Sandstrom, B. E.; Graustrom, M.; Bienvenu, P.; Marklund, S. L. *Biol. Trace Elem. Res.* **1995**, *47* (*1*−*3*), 29.

(91) Yamazaki, I.; Piette, L. H. *J. Am. Chem. Soc.* **1991**, *113*, 7588.

(92) (a) Kim, J.; Harrison, R. G.; Kim, C.; Que, L. Jr. *J. Am. Chem. Soc.* **1996**, *118*, 4373. (b) Menage, S.; Wilkinson, E. C.; Que, L. Jr.; Fontecave, M. *Angew. Chem., Int. Ed. Engl.* **1995**, *34*, 203. (c) Lubben, M.; Meetsma, A.; Wilkinson, E. C.; Feringa, B.; Que, L. Jr. *Angew. Chem., Int. Ed. Engl.* **1995**, *34*, 1512.

(93) (a) Nam, W.; Ho, R.; Valentine, J. S. *J. Am. Chem. Soc.* **1991**, *113*, 7052. (b) Valentine, J. S.; Burstyn, J. N.; Margerum, L. D. In *Oxygen Complexes and Oxygen Activation by Transition Metals*; Martell, A. E., Sawyer, D. T., Eds.; Plenum Press: New York, 1988; pp 175−187. (c) Valentine, J. S.; Vanatta, R. B.; Margerum, L. D.; Yang, Y. In *The Role of Oxygen in Chemistry and Biochemistry*; Ando, W., Moro-Oka, Y., Eds.; Elsevier Science: Amsterdam, 1988; pp 175−184.

(94) (a) Guajardo, R. J.; Hudson, S. E.; Brown, S. J.; Mascharak, P. K. *J. Am. Chem. Soc.* **1993**, *115*, 7971. (b) Nguyen, C.; Guajardo, R. J.; Mascharak, P. K. *J. Am. Chem. Soc.* **1996**, *35*, 6273.

(95) Barton, D. H. R.; Doller, D. *Acc. Chem. Res.* **1992**, *25*, 504.

(96) (a) Balasubramanian, P. N.; Bruice, T. C. *J. Am. Chem. Soc.* **1986**, *108*, 5495. (b) Balasubramanian, P. N.; Bruice, T. C. *Proc. Natl. Acad. Sci. U.S.A.* **1987**, *84*, 1734.

(97) (a) Lee, S. K.; Nesheim, J. C.; Lipscomb, J. D. *Biol. Chem.* **1993**, *268*, 21569. (b) Liu, K. E.; Wang, D.; Huynh, B. H.; Edmondson, D. E.; Salifoglou, A.; Lippard, S. J. *J. Am. Chem. Soc.* **1995**, *116*, 7465. (c) Lee, S. K.; Fox, B. G.; Froland, W. A.; Lipscomb, J. D.; Münck, E. *J. Am. Chem. Soc.* **1993**, *115*, 6450.

(98) Brown, C. A.; Remar, G.; Musselman, R. L.; Solomon, E. I. *Inorg. Chem.* **1995**, *34*, 688.

(99) Koppenol, W. H.; Liebman, J. F. *J. Phys. Chem.* **1984**, *88*, 99.

(100) Corina, D. L.; Miller, S. L.; Wright, J. N.; Akhtar, M. *J. Chem. Soc. Chem. Commun.* **1991**, 782.

(101) (a) Sisemore, M. F.; Burstyn, J. N.; Valentine, J. S. *Angew. Chem. Engl. Ed.* **1996**, *35*, 206. (b) Selke, M.; Sisemore, M. F.; Valentine, J. S. *J. Am. Chem. Soc.* **1996**, *118*, 2008. (c) Sisemore, M. F.; Selke, M.; Burstyn, J. N.; Valentine, J. S. *Inorg. Chem.* **1997**, *36*, 979. (d) Selke, M.; Valentine, J. S. *J. Am. Chem. Soc.* **1998**, *120*, 2652. For a review of other ferric−heme−peroxide chemistry see ref 5a.

(102) (a) Sam, J. W.; Tang, X. J.; Peisach, J. *J. Am. Chem. Soc.* **1994**, *116*, 5250. (b) Westre, T. E.; Loeb, K. E.; Zaleski, J. M.; Hedman, B.; Hodgson, K. O.; Solomon, E. I. *J. Am. Chem. Soc.* **1995**, *117*, 1309.

(103) (a) Rana, T. M.; Meares, C. F. *J. Am. Chem. Soc.* **1990**, *112*, 2457. (b) Rana, T. M.; Meares, C. F. *J. Am. Chem. Soc.* **1991**, *113*, 1859. (c) Rana, T. M.; Meares, C. F. *Proc. Natl. Acad. Sci. U.S.A.* **1991**, *88*, 10578.

(104) Bach, R. D.; Su, M. D.; Andre, J. L.; Schlegel, H. B. *J. Am. Chem. Soc.* **1993**, *115*, 8763.

Acknowledgment. This research is supported by the National Institute of Health (GM40392). F.N. thanks the Deutsche Forschungsgemeinschaft for a postdoctoral fellowship and Dr. Kiyoshi Fujisawa (Tokio Institue of Technology) for a gift of $H_2{}^{18}O_2$. Drs. Thomas Brunold and Elna Pidcock are acknowledged for help in obtaining and analyzing the resonance Raman spectra and for stimulating discussions.

Supporting Information Available: Cartesian coordinates used for MO calculations, VTVH-MCD data for bands 1 and 2, analytical solution of the force field, list of contributions to the calculated *D* and *E/D* values, parameters used in the Morse fits in Figure 11, study of the sensitivity of calculated state energies to the size of the CI space, and a simple model explaining the C-terms signs for bands 3 and 4 (15 pages, print/PDF). See any current masthead page for ordering information and Web access instructions.

JA981561H